Catena 228 (2023) 107171

Contents lists available at ScienceDirect

Catena

journal homepage: www.elsevier.com/locate/catena

Pedogenesis at the coastal arid-hyperarid transition deduced from a Late Quaternary chronosequence at Paposo, Atacama Desert

Janek Walk [a,b,*], Philipp Schulte [a], Melanie Bartz [c,d], Ariane Binnie [e,f], Martin Kehl [d], Ramona Mörchen [g], Xiaolei Sun [h], Georg Stauch [a], Christopher Tittmann [a], Roland Bol [h,i], Helmut Brückner [d], Frank Lehmkuhl [a]

[a] Department of Geography, RWTH Aachen University, 52056 Aachen, Germany
[b] Department of Geography and Regional Research, University of Vienna, 1010 Vienna, Austria
[c] Institute of Earth Surface Dynamics, University of Lausanne, 1015 Lausanne, Switzerland
[d] Institute of Geography, University of Cologne, 50674 Cologne, Germany
[e] Institute of Neotectonics and Natural Hazards, RWTH Aachen University, 52056 Aachen, Germany
[f] Institute of Geology and Mineralogy, University of Cologne, 50674 Cologne, Germany
[g] Institute of Crop Science and Resource Conservation, University of Bonn, 53115 Bonn, Germany
[h] Agrosphere (IBG-3), Institute of Bio- and Geosciences, Forschungszentrum Jülich GmbH, 52428 Jülich, Germany
[i] School of Natural Sciences, Environment Centre Wales, Bangor University, Bangor, United Kingdom

ARTICLE INFO

Keywords:
South America
Pacific Coast
Desert soils
Pedogenic processes
Chronosequences
Exposure age

ABSTRACT

Under hyperarid climate conditions, pedogenesis is driven by the atmospheric deposition and subsequent accumulation of easily to moderately soluble salts forming extreme types of Aridisols. In contrast, the processes and timescales of soil formation in coastal desert environments are as yet not well understood. Therefore, a soil chronosequence at the arid-hyperarid transition in the south-central coastal Atacama Desert is investigated. We measured physicochemical soil parameters of shallow soil profiles on four generations of a multi-stage alluvial fan system, assisted by micromorphological analysis, allowing to deduce the soil-forming processes. We further established a geochronological framework by applying ^{10}Be cosmogenic nuclide exposure dating on the abandoned surface generations, which allowed to infer the timescales for soil formation. The results indicate initial yet clearly identifiable pedogenesis occurring since MIS 5e–c. Along the Late Quaternary chronosequence, physicochemical soil properties show decreasing trends with growing age for the median grain size, salinity, long-term pH development, and $CaCO_3$ contents. Contrarily, organic carbon, the ratio of organic to total phosphorus, the redness, and the contents of total and poorly crystalline pedogenic iron oxides tend to increase with age. This provides evidence for soil formation under an arid to hyperarid coastal climate characterized by (i) redistribution of salts by leaching causing topsoil desalinization; (ii) decalcification coupled with (iii) dealkalinization in totally decalcified horizons; (iv) accumulation of soil organic matter; (v) initial rubification through formation of pedogenic iron oxides (i.e. hematite); and (vi) initial loamification that, in turn, might have impeding effects on the translocation of soil constituents on timescales larger than 10^5 a. Furthermore, *in situ* pedogenesis might be superimposed considerably by aeolian dust influx. At Atacama's south-central coast, the state of pedogenic alteration scales with the cumulative precipitation received throughout the entire Late Quaternary, yet evolved strongest between MIS 5 and the MIS 4/3-transition.

* Corresponding author at: Department of Geography and Regional Research, University of Vienna, 1010 Vienna, Austria.
E-mail addresses: janek.walk@univie.ac.at (J. Walk), philipp.schulte@geo.rwth-aachen.de (P. Schulte), melanie.bartz@unil.ch (M. Bartz), ariane.binnie@uni-koeln.de (A. Binnie), kehlm@uni-koeln.de (M. Kehl), ramona.moerchen@uni-bonn.de (R. Mörchen), xi.sun@fz-juelich.de (X. Sun), georg.stauch@geo.rwth-aachen.de (G. Stauch), christopher.tittmann@kamp-lintfort.de (C. Tittmann), r.bol@fz-juelich.de (R. Bol), h.brueckner@uni-koeln.de (H. Brückner), flehmkuhl@geo.rwth-aachen.de (F. Lehmkuhl).

https://doi.org/10.1016/j.catena.2023.107171
Received 28 December 2022; Received in revised form 10 March 2023; Accepted 13 April 2023
Available online 5 May 2023

1. Introduction

On a global scale, the types and rates of soil-forming processes are primarily linked to the climatic setting, given the parent material and topographic setting are comparable. This is also reflected in a dominance of climate as a pedogenic factor in soil classification (e.g., Gray et al, 2011; Bockheim et al., 2014). In deserts, the limited availability of water governs the biotic activity and pedogenic processes, which are associated with the relocation and leaching of soil constituents as well as the recrystallization of minerals. Lack of precipitation in relation to high evapotranspiration inhibits eluviation of easily to moderately soluble minerals. As a consequence, soils in deserts are characterized by secondary accumulation of $CaCO_3$ (calcic), $CaSO_4{\cdot}2H_2O$ (gypsic), SiO_2 (duric) and more soluble salts (salic), mainly NaCl, in specific horizons (Nettleton and Peterson, 1983; Finstad et al., 2014; IUSS Working Group WRB, 2022). According to the diagnostic soil taxonomy of the United States Department of Agriculture (USDA), such desert soils are summarized as Aridisols and further defined by their diagnostic horizons (Soil Survey Staff, 1999), while equivalent soil types following the current version of the World Reference Base for Soil Resources cover the Reference Soil Groups Calcisols, Gypsisols, Durisols, and Solonchaks (IUSS Working Group WRB, 2022).

Soil formation under hyperaridity – defined according to the UNEP by an Aridity Index <0.05 (Middleton and Thomas, 1997) – has received considerable attention throughout the last two decades, with a strong focus on the Atacama Desert as it is the oldest and driest non-polar desert on Earth, which is often regarded as a terrestrial equivalent for a Mars-like environment (e.g., Ewing et al., 2006; Amundson et al., 2012; Fletcher et al., 2012; Valdivia-Silva et al., 2012; Finstad et al., 2014, Mörchen et al., 2019; Fuentes et al., 2022a). Receiving <5 mm of mean annual precipitation (MAP) in most parts of the Atacama, and even less in its hyperarid core (Houston, 2006), some extreme types of Aridisols have developed, i.a., featuring horizons cemented by gypsum but also by halite (NaCl; indurated salic horizon) and horizons enriched with nitratine ($NaNO_3$; nitric horizon) (Ewing et al., 2006; Finstad et al., 2014). Dust is widely recognized as parent material for synsedimentary pedogenesis (Ewing et al., 2006, Wang et al., 2014). Thus, atmospheric deposition of salts is the principal source of exogenous minerals required for the formation of crusts (Ewing et al., 2008; Wang et al., 2014; Li et al., 2019; Arens et al., 2021; Arenas-Díaz et al., 2022). Up to elevations of ~1,200 m above sea level (a.s.l.), salts principally originate from the Pacific and are transported inland in form of marine aerosols and by inland penetration of coastal fog (Rech et al., 2003; Voigt et al., 2020; Arenas-Díaz et al., 2022). In addition, local entrainment has been found to contribute significantly to the atmospheric deposition of insoluble minerals (Wang et al., 2014). However, although the barren surfaces of the Atacama Desert are prone to wind erosion, deflation is limited due to the rare occurrence of dust storms (Reyers et al., 2019; Arenas-Díaz et al., 2022). Closely related to the limited biotic activity and very sparse to absent vegetation cover in the interior desert, organic carbon (C_{org}) contents in top soils rarely exceed 0.1%; yet spatial variability is high and significantly increased C_{org} contents can be found in the subsoil (Valdivia-Silva et al., 2012; Mörchen et al., 2019 and references therein). Despite its hyperarid climate and low soil organic carbon stocks, habitats for various specially adapted microorganisms have been found in soil crusts, subsurface soils, and in association with specific minerals (e.g., Kuhlman et al., 2008; Azua-Bustos et al., 2011, 2012, 2015; Parro et al., 2011; Wierzchos et al., 2011; Warren-Rhodes et al., 2019; Knief et al., 2020; Fuentes et al., 2022a). Towards the southern Atacama Desert, south of 25°S, effects of increasing precipitation are expressed in higher vegetation density and soil CO_2 concentration, explaining the decline of sulphate content in soils while secondary carbonates become dominant (Quade et al., 2007; Amundson et al., 2012).

In contrast to the processes and timescales of soil formation under continental hyperaridity, very little understanding has been gained as yet about the pedogenesis at the coasts of arid to hyperarid deserts. Such environments are present on four continents; i.e., in southwestern North America, western South America, and along the coasts of North, East, and Southwest Africa, as well as the Arabian Peninsula (Feng and Fu, 2013; Trabucco and Zomer, 2019). Furthermore, the environmental conditions at the coast significantly differ from those further inland due to the direct vicinity to the sea acting as a source of moisture and minerals. In case of the Atacama Desert, the coast receives precipitation up to one order of magnitude higher than the interior (Houston, 2006; Fick and Hijmans, 2017), and is characterized by a higher air humidity and more frequent occurrence of fog events (Cereceda et al., 2002, 2008; Schween et al., 2020; Walk et al., 2022), which enables the growth of specially adapted Loma vegetation (Schulz, 2009; Schulz et al., 2011). In addition, the coast receives much more atmospheric salts mainly due to sea spray (Rech et al., 2003; Wang et al., 2014). Accordingly, Walk et al. (2022) showed that the processes and rates of weathering are specific for the coast and comprise the formation of weathering rinds and clast breakdown dominantly by salt weathering. This ultimately results in fully developed desert pavements on a Late Pleistocene timescale. Hence, we hypothesize significant effects of the coastal environment also on pedogenic processes, which have been studied only poorly until now.

Along a W-E transect within the Paposo catchment at ~25°S, Mörchen et al. (2019) and (2021) assessed the soil organic carbon stocks and plant-specific *n*-alkane distributions, respectively, whereupon the site located most closely to the coast is at an altitude of 600 m a.s.l. (Fig. 1a). Closely related to the availability of moisture due to fog, elevated C_{org} contents (>0.2%) were found up to ~6 km inland and 900 m a.s.l. (Mörchen et al., 2019). In this zone, the signatures of *n*-alkanes in the soil clearly reflect fog-driven formation of soil organic matter (SOM), while SOM above 1200 m a.s.l. originate from plants fed by rain (Mörchen et al., 2021). At a tributary-junction fan situated a few hundred metres above the extent of the advective fog, Moradi et al. (2020) further analysed the colloidal phosphorus and found that the vertical distribution largely varies between two fan sections with different formation ages. The only study assessing a broader range of physicochemical soil parameters at the coast of the Atacama Desert, was recently conducted by Fuentes et al. (2022b) to evaluate the effects of altitude and coastal fog on soil properties along a soil catena at the southern hillslope of the Morro Moreno at ~23.5°S/70.6°W.

As a first study, and in order to systematically assess the processes and timescales of pedogenesis at the coastal arid-hyperarid transition, we investigated a soil chronosequence across a multi-stage alluvial fan located in the western south-central Atacama Desert at the outlet of the Paposo catchment (Fig. 1). We assessed physicochemical top and bottom soil parameters on four generation of the fan system, assisted by a selective micromorphological study. Constituting the parent material, preserved sediments at the coast of either terrestrial or marine origin were predominantly deposited during the Late Pleistocene or Holocene but feature considerable spatial variability in their depositional ages (Bartz et al., 2020a). We, thus, further established a site-specific geochronological framework based on ^{10}Be cosmogenic nuclide exposure dating of the abandoned fan generations. By applying the chronosequence concept (Stevens and Walker, 1970), the effects of the soil-forming factor time on the pedogenic processes can then be evaluated. As the palaeoenvironmental setting varied throughout the Late Quaternary (e.g., Calvo et al., 2001; Stuut and Lamy, 2004; Vargas et al., 2006; Bartz et al., 2020a), the soil chronosequence at the coastal alluvial fan (CAF) Paposo serves as a complementary palaeoenvironmental archive.

2. Study area

The hyperarid Atacama Desert ranges from ~15°S to ~30°S, is largely situated >1000 m a.s.l., and consists of a longitudinal succession of mountain ranges, valleys, and intramontane basins. East of the steep

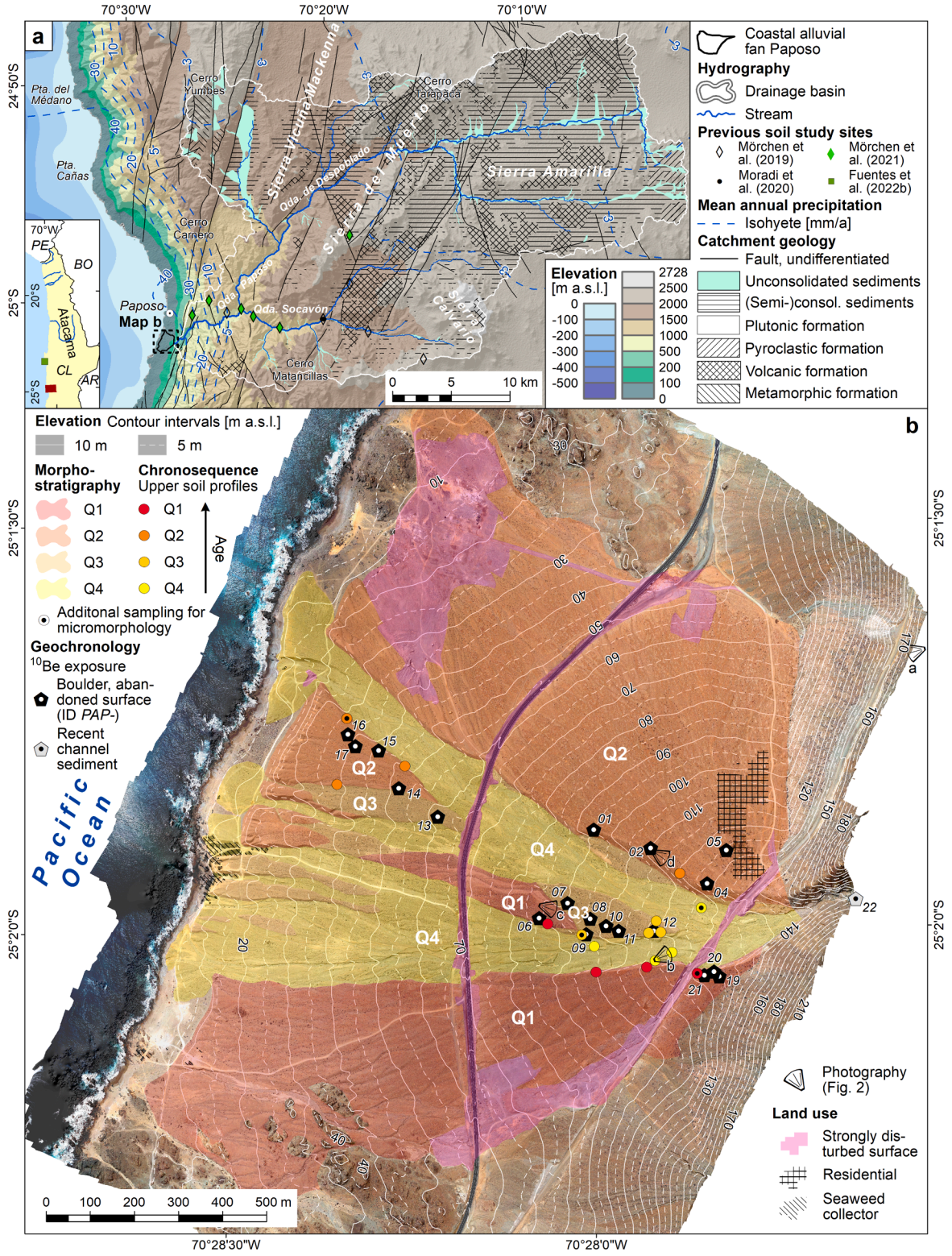

Fig. 1. (a) Regional overview map of the coastal alluvial fan (CAF) Paposo and its catchment within the Coastal Cordillera, located in the southern central Atacama Desert; elevation data (≥0 m a.s.l.) and hydrography based on SRTM 1″ Global (USGS, 2014); bathymetry (<0 m a.s.l.) after GEBCO_2014 Grid (BODC, 2014); sites of previous studies on soils in the Paposo catchment (Mörchen et al., 2019, 2021; Moradi et al., 2020) and along the coast of northern Chile (Fuentes et al., 2022b); mean annual precipitation according to Fick and Hijmans (2017); catchment geological setting after Álvarez et al. (2016) and Escribano et al. (2013) for the area north and south of 25°S, respectively. (b) Aerial imagery map of the CAF Paposo from March 2018 (further information provided by Walk, 2022) showing the fan's relief (in m a.s.l.), morphostratigraphy, soil sample sites classified by colour according to the surface generations (Q4–Q1) with those highlighted that were additionally sampled for micromorphological analysis, sample locations for successfully analysed ^{10}Be cosmogenic nuclide exposure dating, and areas directly affected by land use.

Coastal Cliff, which presents the prominent western flank of the Coastal Cordillera, a narrow, mostly ~1 to ~3 km wide coastal plain hosts a low-altitude environment characterized by distinct climatic and geomorphological processes (e.g., Cereceda et al., 2008; Hartley et al., 2005; Walk et al., 2020, 2022). To investigate the processes and timescales of soil formation in a coastal desert environment, we selected a single, laterally unconfined CAF located in the western south-central Atacama Desert, ~2 km south of the small town Paposo (25.03°S/70.47°W). Fed by a ~63 km long feeder channel that drains a 780 km^2 large catchment, the multi-phase CAF is directly coupled to its source area and presents an optimal archive for a chronosequence study (Fig. 1).

2.1. Geological setting

Aligned along the forearc region of the Central Andes, the Coastal Cordillera of northern Chile evolved from uplift and erosion of a Mesozoic magmatic arc (Scheuber and González, 1999; González et al., 2003; García-Pérez et al., 2018; Oliveros et al., 2018). The Coastal Cordillera is predominantly composed of the Jurassic, andesitic-basaltic La Negra formation, intercalated with pyroclastic breccia and subsequently intruded by granitoid plutonic complexes (Coira et al., 1982; Hartley et al., 2000; Haschke et al., 2002; Walk et al., 2020). In view of the large catchment area, the source-area lithology of the CAF Paposo is diverse (Fig. 1a). While the plateau-like upstream region mostly comprises the volcanic La Negra formation and Miocene to Pliocene (semi-) consolidated alluvial sediments filling the wide and shallow valleys, the middle and lower reaches are dominated by the Middle to Upper Jurassic intrusive Matancilla complex of granodioritic/dioritic composition (Escribano et al., 2013; Álvarez et al., 2016). Furthermore, metasediments of the Palaeozoic accretionary Chañaral Epimetamorphic Complex crop out in the northwest of the catchment (Álvarez et al., 2016; Creixell et al., 2016).

Major faults crossing the catchment include the Paposo, Yumbes, El Jote, and Quebrada Grande Faults (Fig. 1a; Escribano et al., 2013; Álvarez et al., 2016). Featuring NNE–SSW to NE–SW orientations, all are related to the active Atacama Fault Zone which represents the first-order tectonic element structuring the Coastal Cordillera (Scheuber and González, 1999; Grocott and Taylor, 2002; Allmendinger and González, 2010). As a result of the prominent tectonic segmentation, Late Quaternary uplift at the south-central coast features a large spatial variability expressed in rates between 0.1 ± 0.03 and 0.48 ± 0.09 m/ka (Bartz et al., 2020a). The CAF, however, is not directly affected by crossing faults. The sudden transition from the CAF source area to the sink – that is the coastal plain – is determined by the base of the Coastal Cliff (~110 m a.s.l.). Valid for most segments of the coast in northern Chile, last marine overprinting at the cliff base has been dated by extrapolation of re-appraised Quaternary uplift rates to either the marine isotope stage (MIS) 9 (~320 ka) or 11 (~400 ka) (Regard et al., 2010).

2.2. Modern and past climatic setting

While the interior Atacama Desert, including the upper and middle reaches of the Paposo catchment, receives MAP <5 mm (Houston, 2006), the coast at about 25°S is characterized by a MAP exceeding 30 mm (Fig. 1a; Fick and Hijmans, 2017). The coastal plain at Paposo is in the transition between an arid and hyperarid climate (Trabucco and Zomer, 2019). Precipitation features high inter-annual as well as seasonal variability, the latter being expressed in a distinct winter dominance (Supplementary Fig. SF1; Houston, 2006; Reyers et al., 2021). Low-intensity drizzle constitutes the majority of precipitation events (Cereceda et al., 2008; Schween et al., 2022). Soil water monitoring in 10 cm depth over a period of 19 months at the meteorological station Caleta Sur de Punta Grande, located 9 km south of the CAF Paposo, revealed that drizzle and rainfall events <0.5 mm do not have an effect on the volume water content at 10 cm depth (Supplementary Fig. SF2; Hoffmeister, 2018). Events ≥3 mm are required to cause a sudden soil moisture increase that allows for percolation in a sandy soil and were detected a few times per year (Hoffmeister, 2018). In contrast, strong rainfall events capable of activating alluvial fans (≥20 mm) at the coast around Paposo have recurrence intervals of a single to few decades (Walk et al., 2020). Such events originate from extratropical frontal systems (Vuille and Ammann, 1997; Garreaud et al., 2009) or cut-off lows (Fuenzalida et al., 2005; Bozkurt et al., 2016; Jordan et al., 2018; Rondanelli et al., 2019; Reyers and Shao, 2019). A strong maritime impact on the coastal climate is further reflected in low diurnal variabilities of both air temperature and relative humidity (Supplementary Fig. SF1; Cáceres et al., 2007; Cereceda et al., 2008; Schween et al., 2020).

In addition to inducing drizzle, the Coastal Cordillera's orographic effect by blocking the Pacific stratocumulus deck is concomitant with a high occurrence frequency of advective fog between the lifting condensation level and the capping inversion, which corresponds in the study area at 25°S to an altitude of ~400 to ~950 m a.s.l. (Cereceda et al., 2002, 2008; Garreaud et al., 2008). The fog is considered the main source of moisture along the coast of the Atacama Desert, which enables the growth of specifically adapted Loma vegetation. At Paposo, comparatively dense plant cover of 25 to >40% is present between ~400 and ~730 m a.s.l., while the CAF, situated entirely below the lower boundary of frequent fog occurrence, is sparsely vegetated (>5–15%) down to sea level (Fig. 2; Rundel and Mahu, 1976; Rundel et al., 1991; Schulz, 2009).

Throughout the Quaternary, the Atacama Desert has remained hyperarid, though many short-lived phases of wetter conditions occurred (e.g., Placzek et al., 2010; Jordan et al., 2014, Ritter et al., 2019; May et al., 2020; Medialdea et al., 2020). Based on increased Late Pleistocene alluvial fan activity along the coast, wetter intervals have been constrained for 95–80 ka, 60–45 ka, and 35–20 ka and interpreted as a result of atmospheric changes in the SE Pacific (Bartz et al., 2020a). Accordingly, several phases of enhanced pluvial activity during MIS 5 to MIS 2 can be inferred from increased input of terrestrial clastics into a marine offshore sediment record at ~27°S (Stuut and Lamy, 2004). In particular, a wetter climate deduced for the Last Glacial Maximum (LGM, MIS 2) is in agreement with both a higher occurrence frequency of cut-off lows modelled by Reyers and Shao (2019) and a strong intensification of chemical weathering observed by Walk et al. (2022) at the CAF Guanillos (~22°S). It is argued that lower sea surface temperatures (SST) induce northward migration of extratropical fronts, caused by a weakening of the Walker circulation (Stuut and Lamy, 2004). At ~17°S, a record of SE Pacific SST since MIS 11 is preserved in a marine core and shows relative SST minima during glacials (Calvo et al., 2001).

2.3. Coastal alluvial fan morphology and stratigraphy

The single CAF at Paposo is, apart from a small segment in its northern-lateral extent, unconfined by other fan systems and, thus, developed a typical semi-conoidal shape radiating from its apex at ~140 m a.s.l. to the Pacific shoreline (Fig. 1b; Fig. 2a). The main channel trenched the entire alluvial fan and features incision of up to 10 m in the most proximal section before splitting into two major arms that further diverge downstream (Fig. 1b). Such as most alluvial fans along the coast of the Atacama Desert (Walk et al., 2020), the distal section has been eroded by littoral processes, resulting in a Holocene coastal cliff exceeding 10 m in height along the mid-radial course. Radial profiles have a linear shape and are characterized over lengths ranging from ~1.2 to ~1.5 km by average slope angles of 5.5–6°, ~6°, and 6.5–7° in the southern, central, and northern part, respectively.

Based on analysis of aerial imagery and digital surface models derived from surveys conducted with an unoccupied aerial system (Walk, 2022) and ground-truthed by field mapping, the CAF Paposo was subdivided into four morphostratigraphic units (Q1 to Q4; Fig. 1b). Representing a succession of progradation, Q1 to Q3 were formed as

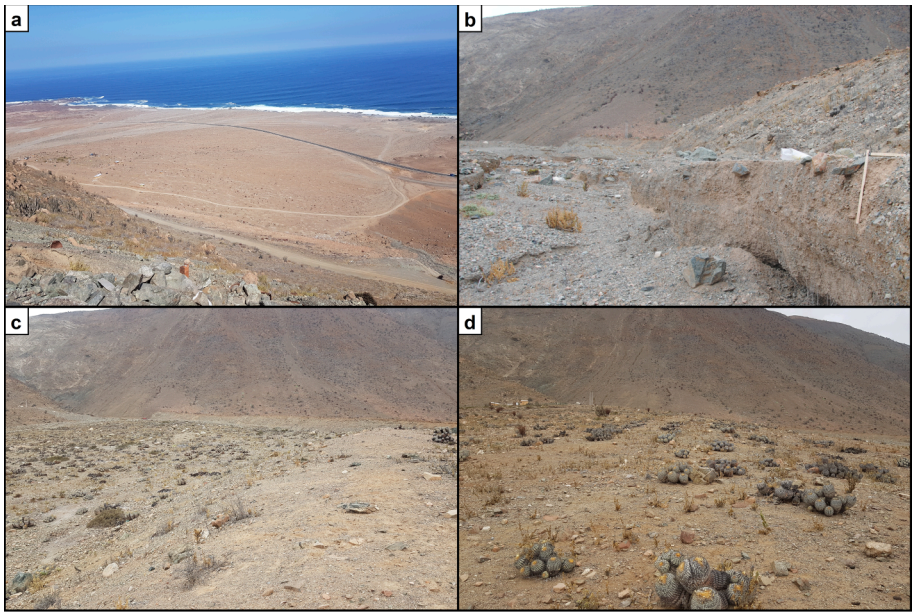

Fig. 2. Photographs of (a) the entire semi-conoidal coastal alluvial fan Paposo (oblique downstream view); (b) the active incised main channel including a ~1 m high edge of a sub-recent terrace (Q4, upstream view); (c) the ~3 m high, prominent terrain step between the (left) second youngest (Q3) and (right and background) oldest (Q1) surface generations (upstream view); (d) the proximal segment of the second oldest generation (Q2, upstream view). Photography locations and viewing directions are indicated in Fig. 1b; photographer: (a–d) J. Walk.

stages of terminal aggradation, each abandoned in the course of subsequent progradation. While Q1 and Q2 comprise the majority of the fan area, Q3 apparently evolved along the central fan by either aggradation or erosion, following deep incision into the fan cone as evidenced by a prominent terrain step between Q1 and Q3 (Fig. 1b; Fig. 2c). Preservation of Q3 is limited to small remnants due to the incision of the youngest generation Q4. Note that Q4 includes the active beds of the main channel arms but also several sub-recent, inactive channels, terraces with heights of up to ~1 m (Fig. 2b), and fan progradation downstream of the Holocene coastal cliff to the shoreline.

The CAF Paposo is composed primarily of poorly-sorted, clast-supported beds of angular gravels and cobbles in a sandy matrix, resulting from hyperconcentrated flows, and secondarily by ungraded clast-rich lobes typical for non-cohesive debris flows (Fig. 3; cf. Hartley et al., 2005; Bartz et al., 2020a, 2020b). Accordingly, depositional slope angles are lower than those of debris-flow dominated CAF (Hartley et al., 2005; Walk et al., 2020). Moreover, bar-and-swale topography, which is the characteristic result of debris flows (Frankel and Dolan, 2007; Blair and McPherson, 2009; de Haas et al., 2014; Walk et al., 2019, 2022), is mostly absent. Post-depositional reworking might be responsible for denudating the primary bars and swales as well as filling palaeochannels (Fig. 2d; de Haas et al., 2014; Walk et al., 2022). Terminal aggradation of the abandoned fan surfaces came along with extensive embedding of angular boulders sized between a few dm and up to ~1.5 m (Fig. 2c, d; Supplementary Fig. SF3). In contrast, deposits of incised channel floods shaping Q4 are comparatively poor in boulders and partly feature parallel bedding of alternating cm-thick layers of angular gravels and sands (Fig. 2b; Fig. 3). In addition, neither intercalated marine terrace deposits nor layers of aeolian sand – both common facies along the coast of the Atacama Desert (Bartz et al., 2020a) – could be detected along the CAF Paposo.

3. Methods

3.1. Cosmogenic nuclide (^{10}Be) exposure dating

3.1.1. Sampling strategy

We collected and analysed in total 20 surface samples from exposed boulders distributed over the three abandoned CAF surfaces Q3, Q2, and Q1, with the majority located in the proximal segments of the respective generation (Fig. 1b). The top few cm of large debris flow-transported boulders of plutonic lithology were chiselled off (Supplementary

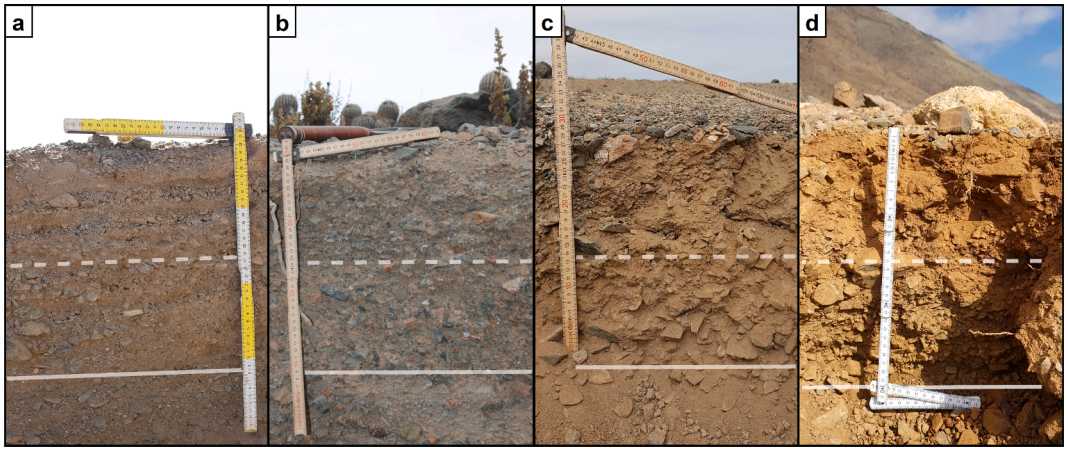

Fig. 3. Photographs of exemplary soil profiles from the CAF Paposo sorted according to the morphostratigraphy and with the two sampling depth intervals 0–15 cm and 15–30 cm marked by the dashed and solid lines, respectively: (a) Q4, 0–15 cm: CL18-097, 15–30 cm: CL18-098; (b) Q3, 0–15 cm: CL18-045, 15–30 cm: CL18-046; (c) Q2, 0–15 cm: CL18-074, 15–30 cm: CL18-075; (d) Q1, 0–15 cm: CL18-034, 15–30 cm: CL18-035. Photographers: (a, d) J. Walk, (b, c) M. Bartz.

Fig. SF3). We considered only boulders apparently embedded in the matrix to minimize the chance of sampling boulders originating from post-aggradational rockfall. Moreover, all samples are from positions considered topographically stable and do not feature major signs of post-depositional erosion (i.e., spalling). Topographic shielding was assessed in the field for each site by measuring the azimuths and inclinations characterizing the local horizons using a precision compass and a clinometer, respectively. In addition, one sample of the recent channel sediment was collected in the feeder channel ~150 m upstream of the fan apex to consider potential ^{10}Be accumulation prior to deposition. In contrast to the exposed boulders, the channel sediment comprises a mixture of fine sands to coarse gravels and reflects in its lithological composition the heterogeneity of the source area (Fig. 1a).

3.1.2. Laboratory analysis and exposure age derivation

Samples for cosmogenic ^{10}Be exposure dating were crushed, ground, and dry sieved to the 250–710 μm grain size fraction. Induced roll magnetic separation was applied to isolate the quartz from the polymineralic samples. The samples were then shaken in a concentrated HCl/H_2SiF_6 mixture and subsequently etched with dilute HF/HNO_3 multiple times overnight in an ultrasonic bath following the procedure after Kohl and Nishiizumi (1992). Assays of the quartz separates were then tested for purity using in-house ICP-OES (inductively coupled plasma – optical emission spectrometry). Seven samples from Q3, eight samples from Q2, four samples from Q1, and the recent channel sediment (PAP-22) yielded enough quartz sufficiently low in Al to allow for clean separation of Be during sample chemistry.

Samples were spiked with ~300 μg of an in-house Be carrier solution, except for samples PAP-12, PAP-14, PAP-20 and PAP-21 that were spiked using a commercial ICP standard solution (Scharlab, 1000 mg/l). Between ~2 and 16 g of pure quartz separate was subsequently dissolved in concentrated HF/HNO_3. Separation of Be from Al and other interfering elements was conducted following the single-step column approach described in Binnie et al. (2015). Samples were prepared in multiple batches, each containing one reagent blank. After co-precipitation of the samples with silver using the procedure of Stone et al. (2004), pressed targets were measured on CologneAMS (Dewald et al., 2013), normalized to the standards of Nishiizumi et al. (2007).

^{10}Be concentrations of the samples were blank corrected for backgrounds following Binnie et al. (2019). Uncertainties comprise the propagated errors in the AMS ratios of the samples and blank as well as an estimated 1% (1σ) uncertainty in ^{9}Be mass added during spiking. We then calculated exposure ages using version 3 (wrapper 3.0.2, constants 3.0.4) of the online tool originally named CRONUS-Earth calculator (https://hess.ess.washington.edu/math/v3/v3_age_in.html; updated from Balco et al., 2008). Default settings including the ERA40 atmospheric reanalysis data (std flag; Lifton et al., 2014) and the primary calibration dataset by Borchers et al. (2016) were applied. We report exposure ages using the LSDn production rate scaling model of Lifton et al. (2014) and, with regard to the careful selection of sampled boulders, under the assumption of zero erosion. However, we provide the relative sensitivity of the ages to potential erosion using the average of maximum erosion rates for clast and bedrock samples (3.6 m/Ma) assessed by Placzek et al. (2014) for the western Coastal Cordillera.

3.1.3. Statistical treatment of exposure age populations

For statistical detection of outliers in the individual ^{10}Be exposure age populations of each abandoned surface generation and the derivation of total landform ages, we applied the Probabilistic Cosmogenic Age Analysis Tool (P-CAAT, version 2.2, https://kgs.uky.edu/anorthite/pcaat/) published by Dortch et al. (2022). In contrast to alternative approaches commonly used for statistical treatment of TCN age datasets, P-CAAT allows for the choice of statistically distinct, normally distributed subpopulations (component Gaussians) based on evidence by the geomorphic context; in particular, the inferred effects of pre- and post-depositional modifications on the studied surface. The tool accounts for both sample age and geologic uncertainty and isolates the component Gaussians from a cumulative probability density estimation (PDE) using Monte Carlo simulations (Dortch et al., 2022).

As each surface generation can be treated as a single landform, we used internal age uncertainties to generate composite PDEs. P-CAAT results are based on narrow numeric bandwidths and model fits exceeding a 3σ correlation threshold ($R^2 \geq 0.997$). The choice of the bandwidth estimators, the model fits, numeric bandwidths, and the characteristics of the preferred component Gaussians are summarized in Table 1 (see also Supplementary Fig. SF4 for plots showing the distributions of exposure ages, model PDEs, and individual component Gaussian contributions).

For all three surface generations, the youngest end-member component Gaussian enclosing minimum two ages at 2σ was selected. We argue that in the case of the multi-stage CAF Paposo pre-exposure of boulders causing accumulation of 'inherited' cosmogenic nuclides prior to their deposition is the principal geomorphic uncertainty to account for (for more details we refer to section 5.1).

3.2. Soil samples

3.2.1. Sampling strategy

Four shallow, 30 cm deep soil profiles were sampled from each morphostratigraphic unit (Q1–Q4) during March and August 2018 (Fig. 1). On the abandoned surface generations Q1 to Q3, all profiles were dug along the prominent terrain steps formed by subsequent incision, specifically by the main channel. Within the incised channel (Q4), the edges of sub-recent gravel bars preserved as small-scale terrace structures were targeted. In all cases, the profiles were cleaned to remove any material potentially affected by weathering or atmospheric deposition of dust due to direct lateral exposure following incision. Bulk samples were taken for two depth intervals at each profile – between 0 and 15 cm and 15–30 cm and referred to in the following as top and bottom soil, respectively (Fig. 3). Only the matrix material of the

Table 1
P-CAAT model parameters and characteristics of the preferred component Gaussian for each abandoned surface generation (see text for details on the choice of the preferred component Gaussian). (1) Details on the different bandwidth estimators are provided by Dortch et al. (2022); MADD = mean absolute Dortch deviants. (2) n (2σ) = number of ages completely enclosed at 2σ based on their internal uncertainties.

		Surface generation		
		Q3	Q2	Q1
Model	Bandwidth estimator(1)	MADD	Mean	MADD
	R^2	1.000	0.997	1.000
	p value	<0.0001	<0.0001	<0.0001
	Numeric bandwidth [ka]	5.74	7.53	14.78
Preferred component Gaussian	n(2σ)(2)	2	3	2
	Probability height	0.0167	0.0136	0.0098
	Landform age [ka]	59.20	72.96	110.98
	Internal uncertainty [ka]	7.16	10.81	17.38
	External uncertainty [ka]	8.75	12.82	20.44

hyperconcentrated flow and sheet flow deposits was sampled. Coarse clasts were sorted out already in the field. Samples were packed in sterile bags to avoid contamination.

During a field campaign in June 2022, one site per generation was resampled for a selection of soil aggregates (Fig. 1b). They were collected from freshly dug profiles and stored carefully in order to be prepared for micromorphological investigation. We took one sample of encrusted material from the top 3 cm of Q4 (CL22-014), one aggregate sample from 20 to 25 cm below the surface of Q3 (CL22-022), two encrusted aggregates from the upper few cm of Q2 (CL22-017, CL22-020), and on Q1, two reddish-brownish soil aggregates from the depths 20–25 cm (CL22-012) and 25–30 cm (CL22-013).

3.2.2. Laboratory analyses

Prior to any analyses of the bulk soil samples, they were air dried at 35 °C, sieved to <2 mm, and homogenized. A large part of the sedimentological and geochemical analyses were performed at the laboratory of the Chair of Physical Geography and Geoecology at the RWTH Aachen University.

For assessing the particle size distribution, two subsets of each sample between 0.3 and 0.8 g were prepared. Organic matter was removed by treating the samples with 0.7 ml 30% H_2O_2 at 70 °C for several hours. To ensure dispersion of the particles, samples were treated with 1.25 ml 0.1 M $Na_4P_2O_7$ in an overhead shaker for 12 h (DIN ISO 11277, 2002; Schulte et al., 2016). Grain size determination was then performed using a Beckman Coulter LS 13320 Laser Diffraction Particle Size Analyzer applying the Mie theory for grain geometry (Fluid RI: 1.33, Sample RI: 1.55, Imaginary RI: 0.1; cf. Özer et al., 2010; Schulte and Lehmkuhl, 2018). Results for the two subsets were averaged. As an indirect measure of the enrichment by secondary minerals formed in the submicron colloidal grain size fraction, we calculated for each sample the differential grain size distribution applying the Fraunhofer approximation as an alternative optical model to the Mie theory, averaged over the 22 grain size classes ranging from 40 to 311 nm ($\Delta GSD_{\bar{x},40-311\ nm}$; Schulte and Lehmkuhl, 2018).

Soil colour was determined by a Konica Minolta CM-5 spectrophotometer detecting the diffused reflected light under standardized conditions (2° observer angle, standard illuminant C) in the range of visible light (360–740 nm) with a spectral resolution of 10 nm (cf. Eckmeier et al., 2010; Bertrams et al., 2014; Zeeden et al., 2017). Duplicate measurements were conducted on each sample after stirring the material and results were averaged. We used the reflectance data converted into the CIE L*a*b* colour space for further analysis. In the CIE L*a*b* (short CIELAB) system, the extinction of light as luminance is expressed on a scale from black (L* = 0) to white (L* = 100), and colour as chromacity coordinates on scales from green (a* < 0) to red (a* > 0) and from blue (b* < 0) to yellow (b* > 0). In opposition to the Munsell colour system, the CIELAB system is more suitable for quantitative and statistical analyses (Barrón and Torrent, 1986; Viscarra Rossel et al., 2009). We then calculated the widely applied redness index RI_{Lab} introduced by Barrón and Torrent (1986) to quantify the colorimetric effect of iron oxides (e.g., Bertrams et al., 2014; Lucke and Sprafke, 2015; Sahwan et al., 2021).

As a physicochemical parameter proportional to the concentration of soluble salts, the electrical conductivity was assessed in 1:5 soil–water extracts ($EC_{1:5}$) based on the standard procedure described in Rowell (1994). Aliquots of 10 g were mixed with 50 ml distilled water, the extracts then shaken for 90 min, and EC measured after an interception hour in a diluted aliquot of the clear suspension with a WTW LF196 microprocessor conductivity meter. All EC values were normalized to a temperature of 25 °C and saturation extracts (soil:water = 1:1).

For soil pH measurements, 10 g of sample material was suspended in 25 ml of 0.01 M $CaCl_2$. After stirring the aqueous solution four times every 15 min with a glass rod, the pH value was determined using a glass electrode (Knick pH-Meter 766 Calimatic).

C_{org} contents were determined at the Institute of Crop Science and Resource Conservation of the University of Bonn using a Soli TOC Cube (Elementar Analysensysteme) equipped with two combustion units: a dynamic heater able to raise the temperature from ambient to 900 °C and a post combustion zone kept at a constant temperature of 800 °C. About 100 mg of sample were weighed into stainless steel crucibles that were heated prior to analysis to avoid contamination by C residues, before combustion in pure oxygen at a flow rate of 150 ml/min and detection of the formed CO_2 by an infrared detector. C_{org} was determined following the temperature programming described as "temperature-dependent differentiation of total carbon" (DIN 19539, 2016). The analysis was stopped when the maximum integration time of 1800 s was exceeded.

Contents of total phosphorus (P_t), inorganic phosphorus (P_{inorg}), and organic phosphorus (P_{org}) were assessed by treating two sample aliquots of 2 g with 50 ml 0.5 M H_2SO_4 each, of which one was prepared beforehand by ignition in a muffle furnace for one hour at 550 °C in order to analyse only P_{inorg} in contrast to P_t in the air-dried sample. We then measured the concentrations of P_t and P_{inorg} in aqueous solutions by spectrophotometry at 880 nm using ammonium molybdate ($(NH_4)_6Mo_7O_{24}$) and following calibration (DIN EN ISO 6878, 2004). Subsequently, soil P_{org} contents were derived by subtracting P_{inorg} from P_t. For 7 samples (CL18-035, -042, -044, -048, -50, -096, and -100), spectrophotometric measurements were done twice based on independent calibration curves and average values were calculated if deemed reproducible.

We further assessed the $CaCO_3$ content by applying the gas-volumetric SCHEIBLER-procedure. Approximately 1 g of sample material was dissolved in 10% HCl and the volume of released CO_2 was measured (ISO 10693, 1995; Schaller, 2000).

The samples' bulk elemental composition was determined by energy dispersive x-ray fluorescence using an Ametek X-ray Fluorescence Spectrometer (SPECTRO, 2007) and reference material for calibration specified in Schulte et al. (2022). After milling the samples with a planetary ball mill, they were dried at 105 °C for 12 h. 8 g of each sample was mixed with 2 g Fluxana Cereox wax, homogenized by an automated shaker, and pressed to a pellet under a pressure of 10 MPa for 120 s. Each sample was measured twice after rotating the pellet by 90°. Based on the resulting elemental concentrations averaged for each sample, we calculated the Ca/Al ratio as an alternative index for decalcification (Buggle et al., 2011). Infiltrating and percolating water causes leaching of more soluble carbonates in contrast to an enrichment of less soluble Al-silicates in the soil (Mason and Moore, 1982). Dependent on the soil water movement in a similar functional relationship, the ratio (Na + K)/Al was further calculated as an alternative proxy indicating the degree of soil salinization (Sheldon and Tabor, 2009).

For all soil samples, the contents of total free iron oxides (Fe_d) and of the poorly crystalline free iron oxides (Fe_o) were assessed on 2–3 g of sample material each, by extraction with $Na_2S_2O_4$ (Na-dithionite) and $(NH_4)_2C_2O_4$ (ammonium oxalate), respectively (Mehra and Jackson, 1958; Schwertmann, 1959). Reduction to Fe_d followed the adapted procedure according to Holmgren (1967). The concentrations of both reduced Fe_d and Fe_o in the solutions were determined as *ortho*-phenanthrolin ($C_{36}H_{24}FeN_6^{+2}$) complexes by spectrophotometric measurement and calibration at 530 nm. To check for reproducibility, replicate analyses of Fe_d and Fe_o were conducted for 8 samples (CL18-029, -030, and -097 to -102) and results for those samples were averaged.

From the selected soil aggregates, one uncovered thin section of a maximum size of 28 mm × 48 mm and ~30 μm thickness was prepared per sample using epoxy resin under vacuum at the Institute of Geology at the University of Cologne. The thin sections were flatbed-scanned at 1200 dpi using transparent light (TL), under polarized light (XPL), and using reflected light (RL) against a black background, before the scans were investigated at the computer screen at magnifications of up to 25x. A polarization microscope was used for inspection under plane polarized light (PPL) or crossed polarizers (XPL) at magnifications of about 25x to 500x, while oblique incident light (OIL) was applied with a torch to

Table 2
^{10}Be cosmogenic nuclide exposure data of alluvial fan surface clasts and recent channel sediment (Q4). Attribution of samples to surface generations follow the morphostratigraphic model shown in Fig. 1b. The version 3 of the online calculator formerly known as the CRONUS-Earth calculator (https://hess.ess.washington.edu/math/v3/v3_age_in.html; updated from Balco et al., 2008) was used for ^{10}Be exposure age calculation of quartz minerals applying the scaling scheme of Lifton et al. (2014) (LSDn) and assuming zero erosion. h_{SRTM} = sample elevation according to the SRTM 1″ Global by the USGS (2014), d = sample thickness, ρ_g = sample bulk density (values in italics are measured, others are inferred from the petrography), f_{topo} = topographic shielding factor, c(^{10}Be) = blank-corrected concentration of ^{10}Be, at(^{10}Be)$_{blank}$/at(^{10}Be)$_i$ × 100 = percentage of total ^{10}Be atoms measured that are subtracted by the blank correction, Interr = 'internal' uncertainty, Exterr = 'external' uncertainty. Exposure ages (±Interr) highlighted in bold are completely enclosed at 2σ by the preferred component Gaussian (cf. Fig. 4). (1) Erosion sensitivity represents the relative increase in ages when the average of maximum clast and bedrock erosion rates from the western Coastal Cordillera (3.6 m/Ma) after Placzek et al. (2014) are used; note that the samples PAP-01, PAP-17, PAP-20 and PAP-21 appear to be saturated (sat) assuming such erosion rate.

Sample ID	Sample type	Surface generation	Lat [°]	Lon [°]	h_{SRTM} [ma.s.l.]	d [cm]	ρ_g [g/cm^3]	f_{topo}	c(^{10}Be) [at/g × 10^3]	1σ c(^{10}Be) [at/g × 10^3]	at(^{10}Be)$_{blank}$/ at(^{10}Be)$_i$ × 100 [%]	Age ± Interr (Exterr) [ka]	Erosion sensitivity [%](1)
PAP-22	channel sediment	Q4	−25.0328	−70.4607	194	1.5	*2.84*	0.8751	706	32.2	0.3	–	–
PAP-07	boulder (plutonic)	Q3	−25.0328	−70.4672	90	3.5	2.7	0.9921	152	7.14	0.6	**56 ± 2.7(4.3)**	16
PAP-08	boulder (plutonic)	Q3	−25.0331	−70.4667	99	4	2.7	0.9918	275	12.3	0.4	98 ± 4.5(7.5)	31
PAP-09	boulder (plutonic)	Q3	−25.0335	−70.4668	98	4.5	*2.7*	0.9918	222	15.8	4.2	80 ± 5.9(7.6)	25
PAP-10	boulder (plutonic)	Q3	−25.0333	−70.4663	101	2.5	2.7	0.9909	328	16.1	1.0	114 ± 5.7(9.0)	40
PAP-11	boulder (plutonic)	Q3	−25.0334	−70.4660	103	2.5	*2.76*	0.9909	299	24.8	0.4	105 ± 8.9(10.9)	37
PAP-12	boulder (plutonic)	Q3	−25.0334	−70.4653	108	3.5	2.76	0.9883	178	10.4	6.3	**64 ± 3.8(5.4)**	21
PAP-13	boulder (plutonic)	Q3	−25.0310	−70.4701	62	2.5	2.7	0.9961	288	12.5	0.4	104 ± 4.6(7.8)	35
PAP-01	boulder (plutonic)	Q2	−25.0313	−70.4666	92	3	2.8	0.9928	1232	43.9	0.1	461 ± 18.5(35.7)	sat
PAP-02	boulder (plutonic)	Q2	−25.0317	−70.4653	106	1.5	2.87	0.9906	126	8.42	1.7	43 ± 2.9(3.9)	18
PAP-04	boulder (plutonic)	Q2	−25.0324	−70.4640	130	1	2.7	0.9867	194	8.29	1.2	**66 ± 2.9(4.9)**	22
PAP-05	boulder (plutonic)	Q2	−25.0318	−70.4636	126	3	*2.7*	0.9854	230	10.2	1.2	**81 ± 3.7(6.1)**	25
PAP-14	boulder (plutonic)	Q2	−25.0304	−70.4710	49	1	2.87	0.9966	199	14.0	6.9	**72 ± 5.2(6.8)**	25
PAP-15	boulder (plutonic)	Q2	−25.0296	−70.4714	38	3.5	*2.7*	0.9967	368	15.0	1.1	133 ± 5.6(9.9)	51
PAP-16	boulder (plutonic)	Q2	−25.0293	−70.4721	34	4.5	*2.66*	0.9962	401	16.1	0.3	148 ± 6.2(11.0)	57
PAP-17	boulder (plutonic)	Q2	−25.0295	−70.4719	38	2.5	2.87	0.9962	800	38.7	1.8	294 ± 15.3(24.2)	sat
PAP-06	boulder (plutonic)	Q1	−25.0331	−70.4678	85	2	2.7	0.9935	339	14.6	0.2	**118 ± 5.2(8.9)**	42
PAP-19	boulder (quartz vein)	Q1	−25.0343	−70.4638	124	2.5	2.65	0.9800	288	17.7	5.0	**101 ± 6.3(8.8)**	32
PAP-20	boulder (plutonic)	Q1	−25.0342	−70.4639	121	3	*2.87*	0.9822	548	21.1	1.1	189 ± 7.6(14.0)	sat
PAP-21	boulder (plutonic)	Q1	−25.0343	−70.4641	120	3	2.7	0.9822	594	21.0	0.7	203 ± 7.5(14.7)	sat

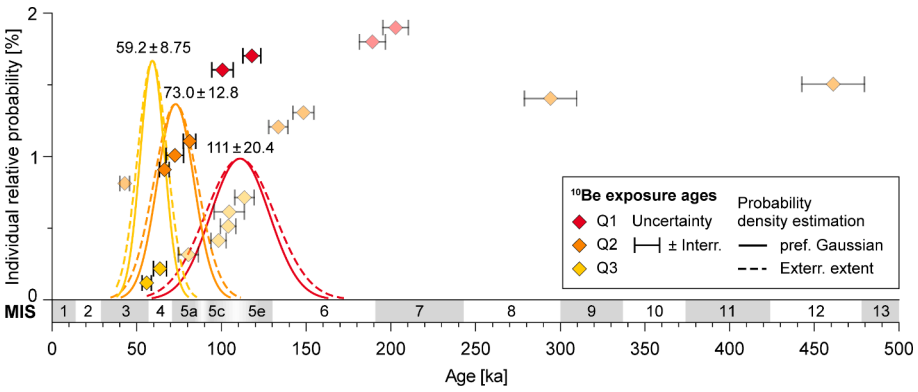

Fig. 4. Individual ^{10}Be exposure ages in rank order for the three abandoned surface generations Q3 to Q1 classified by colour (Q3 – light orange, Q2 – orange, Q1 – red) and displaying their internal uncertainties. Shown are also the individual preferred component Gaussian PDEs, corresponding external uncertainties, and derived total landform ages (± external uncertainties) resulting from the statistical P-CAAT analyses following Dortch et al. (2022) (see also section 3.1.3 for details). Exposure ages highlighted in intense colours are completely enclosed at 2σ by the preferred component Gaussian, while semi-transparent ages can accordingly be considered outliers. Displayed marine isotope stages (MIS) follow Lisiecki and Raymo (2005). (For interpretation of the references to colour in this figure legend, the reader is referred to the web version of this article.)

study opaque features. The different illumination techniques allow identification of mineral and organic constituents down to a grain size of about 5 μm in diameter. Smaller particles comprise the so-called micromass. The characteristics of the pore space, groundmass and pedological features were recorded following the terminology of Stoops (2021). For identification of constituents, atlases and textbooks on soil micromorphology (e.g., Stoops et al., 2018) were consulted.

4. Results

4.1. Morphochronology: ^{10}Be exposure dating

^{10}Be/^{9}Be ratios assessed for the PAP samples lie between 3.31 ± 0.21 × 10^{-14} (PAP-02) and 5.15 ± 0.23 × 10^{-13} (PAP-22), while those of the reagent blanks measured alongside the samples amount to 5.48 ± 2.74 × 10^{-16} (PAP-01, -02, -06, -07, -08, -11, -13, -16), 2.45 ± 1.0 × 10^{-15} (PAP-04, -05, -09, -10, -22), 3.09 ± 0.55 × 10^{-15} (PAP-12, -14, -20, -21), and 1.09 ± 0.33 × 10^{-15} (PAP-15, -17, -19). Blank-corrected concentrations reported for all samples are deemed reliable as blank subtractions make up <7% – for 16 of 20 samples <2% (Table 2). ^{10}Be concentrations of exposed boulders range from 1.26 ± 0.08 × 10^{5} (PAP-02) to 1.23 ± 0.04 × 10^{6} at/g (PAP-01) and the recent channel sediment sample PAP-22 yielded a ^{10}Be concentration of 7.06 ± 0.32 × 10^{5} at/g.

In Table 2, exposure ages are given under the assumption of zero erosion. We report the sensitivity of the ages to erosion ('erosion sensitivity') in form of relative difference and at a rate of 3.6 m/Ma, which can be considered a plausible maximum estimation based on clast and bedrock erosion rates assessed by Placzek et al. (2014) for the western Coastal Cordillera (Table 2). Furthermore, we provide both 'internal' and 'external' uncertainties, representing only the analytical uncertainties in the ^{10}Be concentration measurement in contrast to both analytical and production rate uncertainty (Balco et al., 2008). However, as production rate uncertainties should not be considered for chronologies of individual landforms and based on a single methodological approach (e.g., Dortch et al., 2022), individual exposure ages are displayed using internal age uncertainties (Fig. 4). Results range from 56 ± 2.7 to 114 ± 5.7 ka, 43 ± 2.9 to 461 ± 18.5 ka, and 101 ± 6.3 to 203 ± 7.5 ka for the surface generations Q3, Q2, and Q1, respectively (Table 2).

After statistical treatment of the individual age populations and outlier detection using P-CAAT, preferred component Gaussian PDEs yield total landform ages of 59.2 ± 8.75 ka for Q3 (n = 2), 73.0 ± 12.8 ka for Q2 (n = 3), and 111 ± 20.4 ka for Q1 (n = 2) (Fig. 4). Note that sample age uncertainties are propagated by P-CAAT to result in an external uncertainty (Dortch et al., 2022). Constituting a coherent Late Pleistocene morphochronology, total landform ages significantly differ at 2σ between Q1 and Q2 but only at 1σ between Q2 and Q3. Successive progradation from Q1 to Q3 can, thus, be concluded to have occurred between MIS 5e–c and the transition from MIS 4 to MIS 3 (Fig. 4). Accordingly, main channel incision and formation of Q4 can be constrained to a time span since MIS 3 (~50 ka).

4.2. Pedological results

Physicochemical soil analyses were conducted on the fine earth fraction <2 mm and results are summarized in Table 3. Most samples are comprised of sand and classified as coarse to loamy coarse sand according to the textural classification of the USDA (1987) (Table 3; Fig. 5). A higher contribution of silt and clay, characterizing the samples as (coarse) sandy loam, can be found in 8 samples, mostly originating from Q1. Fining with increasing age of the morphostratigraphic unit is further reflected in the distribution of the median grain sizes (med_x) characterized by arithmetic means decreasing from 584 nm (Q4) to 351 nm (Q1) (Fig. 6a). While the negative trend with growing landform age is highly significant, no significant differences between the top or bottom soils were found for any of the four generations. Enrichment of colloids by secondary mineral formation in the submicron fraction (40–311 nm), is indicated by $\Delta GSD_{\bar{x},40-311\ nm}$ values of ~0.1 to 0.5 vol-‰ for several samples from Q2 and Q1 (Fig. 6b).

Soil salinity varies strongly from low $EC_{1:5}$ <1 dS/m assessed for Q3 and almost all samples of Q1 to $EC_{1:5}$ ranging from ~1 to 10 dS/m and, thus, defining moderately to strongly saline conditions for most soil samples of Q2 and Q4 (Table 3; Fig. 6c). Although changes in the distributions of $EC_{1:5}$ are not consistent with age, the long-term decrease is significant. A very similar pattern along the chronosequence can be observed in the distributions of the elemental ratio (Na + K)/Al, which has been defined by Sheldon and Tabor (2009) as an alternative proxy for soil salinization (Fig. 6i). This suggests that the differences in relative abundance of Na and K is principally dominated by processes enriching or depleting soluble salts in this arid to hyperarid coastal environment.

In contrast, a relatively small range of soil pH values between 7.7 and 8.1 specify slightly to moderately alkaline conditions that remain stable over a timescale from Q4 (<50 ka) to Q2 (73 ± 13 ka) (Fig. 6d). No significant trend with relative age exists along the entire chronosequence as only the soils on the oldest surface generation show pH values in a near-neutral range. On Q1, acidification towards near-neutral pH values affects the top soils slightly stronger than the bottom soils.

The contents of C_{org} are in an overall low order of magnitude, yet they vary largely (Table 3). Q4 features invariably small C_{org} contents <0.13%, while their range and arithmetic means increase with age (Fig. 6e). Despite many samples of Q3, Q2, and Q1 showing low C_{org} contents in the same range as detected for Q4, considerable contents of >0.2% and up to 0.95% were yielded for in total 9 samples on the three abandoned surface generations. Despite a tendency to an age-dependent increase of C_{org}, no significant relationship could be found (Fig. 6e). Furthermore, disproportionally high enrichment of C_{org} in the top versus bottom soil could only be constrained for Q1.

The distribution pattern of organic phosphorus along the

Table 3
Results of physicochemical soil analyses; med_x = median grain size, $\Delta GSD_{\bar{x},40-311\ nm}$ = differential grain size distribution according to Schulte and Lehmkuhl (2018) for the colloidal grain size fraction between 40 and 311 nm, CIELAB luminance value L* and chromacity coordinates a* and b*; RI_{Lab} = redness index after Barrón and Torrent (1986), $EC_{1:5}$ = electrical conductivity in 1:5 soil–water extracts, soil pH value, C_{org} = organic C content, P_{org}/P_t = proportion of organic P in total P, $CaCO_3$ content, Ca/Al ratio, salinization proxy (Na + K)/Al after Sheldon and Tabor (2009), Fe_d = content of dithionite-soluble pedogenic iron, and Fe_o = content of oxalate-soluble pedogenic iron. (1) Subdivisions of sandy textural classes according to Jahn et al. (2006), based on the USDA (1987): CS = coarse sand, LCS = loamy coarse sand, CSL = coarse sandy loam.

Sample ID CL18-	Surface generation	Depth [cm]	Lat [°]	Lon [°]	Tex-ture(1)	med_x [µm]	$\Delta GSD_{\bar{x},40-311\ nm}$ [vol.-‰]	L*	a*	b*	RI_{Lab}	$EC_{1:5}$ [dS/m]	pH	C_{org} [%]	P_{org}/P_t	$CaCO_3$ [%]	Ca/Al	(Na + K)/ Al	Fe_d [g/kg]	Fe_o [g/kg]
039	Q4	0–15	–25.0340	–70.4652	CSL	471	0.000	61.1	4.1	17.3	0.82	10.08	7.91	0.091	0.110	0.48	0.505	0.856	5.13	0.03
040		15–30			CSL	356	0.000	62.5	4.1	17.1	0.70	8.84	8.10	0.086	0.057	1.60	0.517	0.783	5.24	0.02
041	Q4	0–15	–25.0338	–70.4648	CS	632	0.000	59.3	2.5	15.4	0.58	0.24	8.09	0.063	0.079	0.96	0.454	0.537	3.74	0.01
042		15–30			CS	700	0.060	58.9	2.2	14.8	0.54	0.16	7.86	0.063	0.000	1.17	0.420	0.559	3.03	0.01
047	Q4	0–15	–25.0329	–70.4642	LCS	521	0.058	59.3	3.3	17.1	0.77	4.23	7.80	0.106	0.064	0.23	0.591	0.665	4.79	0.02
048		15–30			CS	643	0.006	58.9	2.5	15.6	0.62	2.04	8.01	0.076	0.009	1.52	0.456	0.631	4.13	0.01
097	Q4	0–15	–25.0337	–70.4666	LCS	668	0.082	60.1	3.6	16.9	0.79	3.44	7.85	0.091	0.001	2.06	0.508	0.660	5.76	0.05
098		15–30			LCS	680	0.158	60.4	3.6	17.4	0.76	2.76	7.84	0.127	0.106	1.07	0.487	0.618	4.20	0.07
043	Q3	0–15	–25.0334	–70.4651	CS	606	0.021	55.7	2.7	15.3	0.92	0.22	7.86	0.233	0.174	0.62	0.426	0.532	4.40	0.01
044		15–30			CS	586	0.005	57.6	2.6	15.3	0.72	0.25	8.10	0.132	0.000	0.24	0.471	0.536	4.95	0.01
045	Q3	0–15	–25.0334	–70.4654	CS	568	0.011	54.1	2.7	15.2	1.09	0.24	7.40	0.309	0.057	0.21	0.356	0.543	4.01	0.02
046		15–30			CS	631	0.035	57.4	3.0	16.3	0.85	0.20	7.83	0.187	0.099	0.57	0.370	0.519	4.20	0.01
049	Q3	0–15	–25.0332	–70.4652	CS	577	0.042	52.9	2.8	15.1	1.31	0.81	8.14	0.499	0.017	0.56	0.425	0.581	3.32	0.02
050		15–30			CS	546	0.014	56.4	1.9	14.4	0.58	0.30	7.95	0.087	0.000	0.61	0.404	0.495	4.75	0.03
099	Q3	0–15	–25.0335	–70.4669	CS	516	0.003	57.0	2.8	16.5	0.83	0.11	7.95	0.164	0.022	0.43	0.361	0.517	4.14	0.09
100		15–30			LCS	524	0.021	58.9	3.0	16.8	0.73	0.19	8.08	0.139	0.000	1.18	0.450	0.494	4.41	0.11
051	Q2	0–15	–25.0322	–70.4647	LCS	433	0.149	49.0	5.3	18.9	4.02	3.98	7.69	0.947	0.236	0.11	0.423	0.622	5.68	0.82
052		15–30			LCS	525	0.293	53.6	4.8	18.7	2.07	1.68	7.88	0.413	0.151	0.18	0.347	0.523	5.00	0.04
072	Q2	0–15	–25.0300	–70.4708	LCS	423	–0.017	58.0	3.0	17.6	0.79	0.69	8.02	0.088	0.021	0.00	0.392	0.523	5.15	0.02
073		15–30			CS	489	0.022	56.4	3.7	16.5	1.17	1.04	7.82	0.133	0.049	0.24	0.380	0.535	4.60	0.02
074	Q2	0–15	–25.0290	–70.4721	LCS	491	0.062	56.6	3.8	18.3	1.18	0.54	7.68	0.054	0.088	0.03	0.356	0.522	4.75	0.02
075		15–30			LCS	453	0.024	57.3	3.7	17.2	1.08	2.32	7.83	0.064	0.036	0.45	0.394	0.579	5.06	0.02
076	Q2	0–15	–25.0303	–70.4723	CSL	287	0.203	56.6	4.8	18.7	1.51	7.99	7.74	0.029	0.080	0.00	0.346	0.748	5.42	0.03
077		15–30			LCS	560	0.016	58.2	3.7	16.8	0.96	4.90	7.91	0.031	0.038	0.44	0.454	0.734	4.42	0.02
029	Q1	0–15	–25.0343	–70.4643	CSL	322	0.124	48.4	6.8	20.3	5.57	0.07	6.64	0.817	0.222	0.00	0.270	0.509	9.11	1.53
030		15–30			CSL	311	0.345	49.9	6.8	20.9	4.66	1.04	7.07	0.344	0.137	0.00	0.268	0.505	8.35	0.66
034	Q1	0–15	–25.0341	–70.4654	LCS	310	0.037	50.0	7.5	22.2	5.09	1.81	6.63	0.128	0.034	0.00	0.286	0.550	7.89	0.18
035		15–30			LCS	492	0.000	51.8	5.4	20.2	2.86	1.13	7.88	0.070	0.000	0.00	0.270	0.545	6.17	0.02
095	Q1	0–15	–25.0342	–70.4666	CSL	262	0.025	52.9	6.7	21.1	3.22	0.28	7.45	0.507	0.233	0.00	0.264	0.511	7.10	0.11
096		15–30			CSL	354	0.498	49.9	6.5	20.6	4.38	0.52	7.75	0.129	0.000	0.00	0.244	0.467	4.98	0.04
101	Q1	0–15	–25.0332	–70.4676	LCS	412	0.020	52.4	4.6	18.7	2.29	0.48	7.76	0.497	0.109	0.00	0.338	0.514	5.64	0.23
102		15–30			CSL	346	0.232	52.6	5.2	20.4	2.55	0.21	8.03	0.120	0.132	0.00	0.294	0.477	6.92	0.40

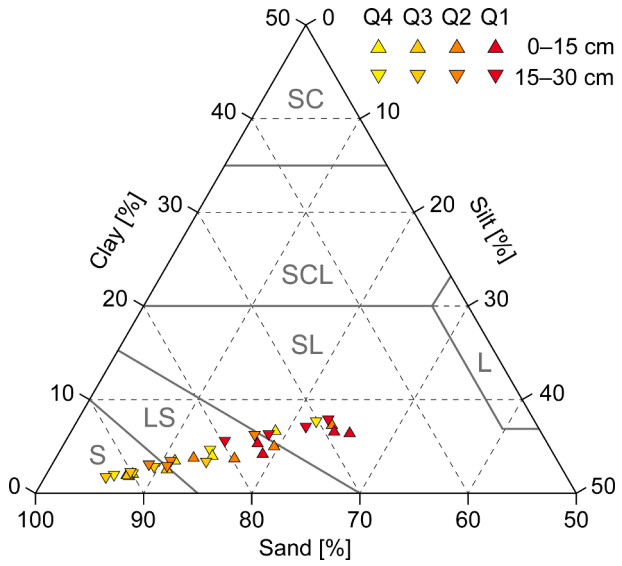

Fig. 5. Soil texture of all individual samples plotted in the sandy subsection (≥50% sand, ≤50 % silt, ≤50 % clay) according to the USDA soil texture classification (USDA, 1987); S = sand, LS = loamy sand, SL = sandy loam, L = loam, SCL = sandy clay loam, S = sandy clay; data plotted using the TRI-PLOT Excel spreadsheet provided by Graham and Midgley (2000). Analysed samples are categorized by colour and shape according to the morphostratigraphic unit and sampling depth interval, respectively.

chronosequence is also highly variable. As both contents of P_{org} and total phosphorus show large ranges from ~0 to 0.43 g/kg and 0.79 to 3.13 g/kg, respectively, P_{org} is further interpreted in relation to P_t. Accordingly, P_{org} contributes on average between ~5% (Q4 and Q3) and 11% (Q1) to the total stock of phosphorus, featuring maximum values of 23–24% but also 8 soil samples containing almost no P_{org} ($P_{org}/P_t < 0.01$) (Table 3; Fig. 6f). Although an increase of both the maxima and arithmetic means of P_{org}/P_t becomes apparent with increasing age of the fan generations, this relationship is not significant (Fig. 6f).

$CaCO_3$ content experiences a consistent and significant, negative trend with increasing landform age (Fig. 6g). Both the ranges and arithmetic means consistently decrease from 0.23–2.06% and 1.14%, respectively, for Q4 to completely decalcified samples of Q1 (Table 3). Strong and steady decrease of $CaCO_3$ in the top soils on Q2, concomitant with a relative enrichment in the bottom soils, is a clear indication for leaching (Fig. 6g). Results on $CaCO_3$ are in close agreement with the elemental ratios Ca/Al shown in a very similar, highly significant decline from on average 0.492 (Q4) to 0.279 (Q1) (Fig. 6h).

Quantified in the CIELAB colour space, differences in the spectrophotometric results indicate an influence of different soil-colouring constituents. The most apparent change of soil colour with age – the visible reddening and browning (Fig. 3) – is constrained quantitatively by a consistent increase of the spectrophotometric Redness Index from average RI_{Lab} of 0.7 for Q4 to 3.83 for Q1 (Table 3; Fig. 6j). The differences between morphostratigraphic units largely grow towards the oldest abandoned surface generation, resulting in a highly significant positive trend with relative age. For Q4, slightly higher RI_{Lab} were detected in the top soils but discrepancies by depth fade with age. As secondary formation of iron oxides – in particular, pedogenic hematite and goethite – are dominating the redness of soils (e.g., Barrón and Torrent, 1986; Sahwan et al., 2021), we examine results of free iron oxides extracted by dithionite (Fe_d) alongside (Table 3). Along the chronosequence, the distributions of Fe_d show a trend that is very similar to the one of RI_{Lab} (cf. Fig. 6j, k). Although samples from Q4 and Q3 contain mostly ~4–5 g/kg Fe_d and have similar distributions, a significant increase becomes apparent and can be attributed to the elevated Fe_d contents of Q2 and Q1, yielding on average, 5.01 and 7.02 g/kg, respectively. In contrast, contents of poorly crystalline iron oxides (Fe_o) are minimal (<0.2 g/kg) in almost all samples from Q4 to Q2. Only Q1 features higher Fe_o contents arising from four samples containing >0.2 to 1.53 g/kg Fe_o.

Complementary to the physicochemical soil properties, micromorphology provides valuable insights into the composition and structure of selected soil samples. Thin section CL22-014 (Fig. 7a), which originates from the surface of the youngest fan generation (Q4), shows a groundmass composed of well-rounded rock fragments, very limited amounts of fine particles (silt and sand) and a grey micromass (silt and clay fraction <5 μm in diameter). The pore space is characterized by simple packing voids, while biopores consisting of chambers and burrows are very rare. A single-grain microstructure is dominant. At the top of the thin section, fine silt and clay particles are concentrated along a thin (<1 mm) undulating microlayer at ~3 mm below surface, resembling in-washed material of a sieving crust (Williams et al., 2018). Apart from the thin crust, pedological features are lacking.

Thin section CL22-022 from a bottom soil of Q3 shares many micromorphological characteristics with CL22-014. However, the porosity is higher and the micromass is less abundant as well as slightly more brownish than in CL22-014 (Fig. 7b). A thin calcite crust covers the base of one of the rock fragments. This crust and the slightly darker colour of the micromass indicate an initial stage of pedogenesis, somewhat more advanced than on Q4.

Soils from the abandoned surface generation Q2 are represented in two thin sections both showing slightly higher contents of fine sand and silt than thin sections from Q3 and Q4. The fine fraction features relatively good sorting, while the groundmass is characterized by a single grain and partly pellicular grain microstructure (Fig. 7c). The faint reddish-brown colour and locally expressed stipple-speckled birefringence-fabric of the micromass suggest an elevated content of pedogenic iron oxides and mobilization of clay, respectively. The presence of some biogenic chambers and burrows can be attributed to bioturbation by soil mesofauna (Kooistra and Pulleman, 2018). At the top of thin section CL22-017, a silt-rich ~5 mm thick structural crust is visible with abundant vesicles in its lower part, which is slightly darker and locally banded, probably representing a washed-in zone (Fig. 7c). The upper part is densely packed and almost devoid of pores. Sedimentary features, such as lamination or graded bedding (Williams et al., 2018), are not present. Another peculiar feature are well accommodated angular rock fragments with rounded outer shape indicative of in-situ breakdown of gravel due to physical weathering.

The two thin sections originating from Q1 are characterized by a reddish-brown colour of the groundmass related to accumulation of pedogenic iron oxides (Fig. 7d). Due to their pigmenting effect, the birefringence-fabric (b-fabric) of the micromass is mostly undifferentiated, but orientation of clay around sand grains has locally resulted in expression of granostriated b-fabric. Close porphyric and chitonic coarse-fine related distribution patterns as well as a clear tendency to formation of subangular blocky soil peds are evident. In addition, thin reddish-brown iron oxide and clay coatings with dotted or cloudy limpidity and diffuse extinction bands are found in few pores including fissures of rock fragments. Moreover, biogenic chambers and channels reflect bioturbation on a microscale. Based on the micromorphological features, samples of Q1 show the strongest imprint of pedogenic alteration.

5. Discussion

A depositional complex such as the CAF Paposo, featuring a morphostratigraphic differentiation into four distinct surface generations, is an exception in the coastal Atacama Desert. Although fans are abundant along the coast, most are either in an advanced state of a single-stage evolution or show one phase of progradation accompanied by incision of the main channel (Walk et al., 2020). Apart from the alluvial fans on the Mejillones Peninsula that extend along a prominent normal fault east

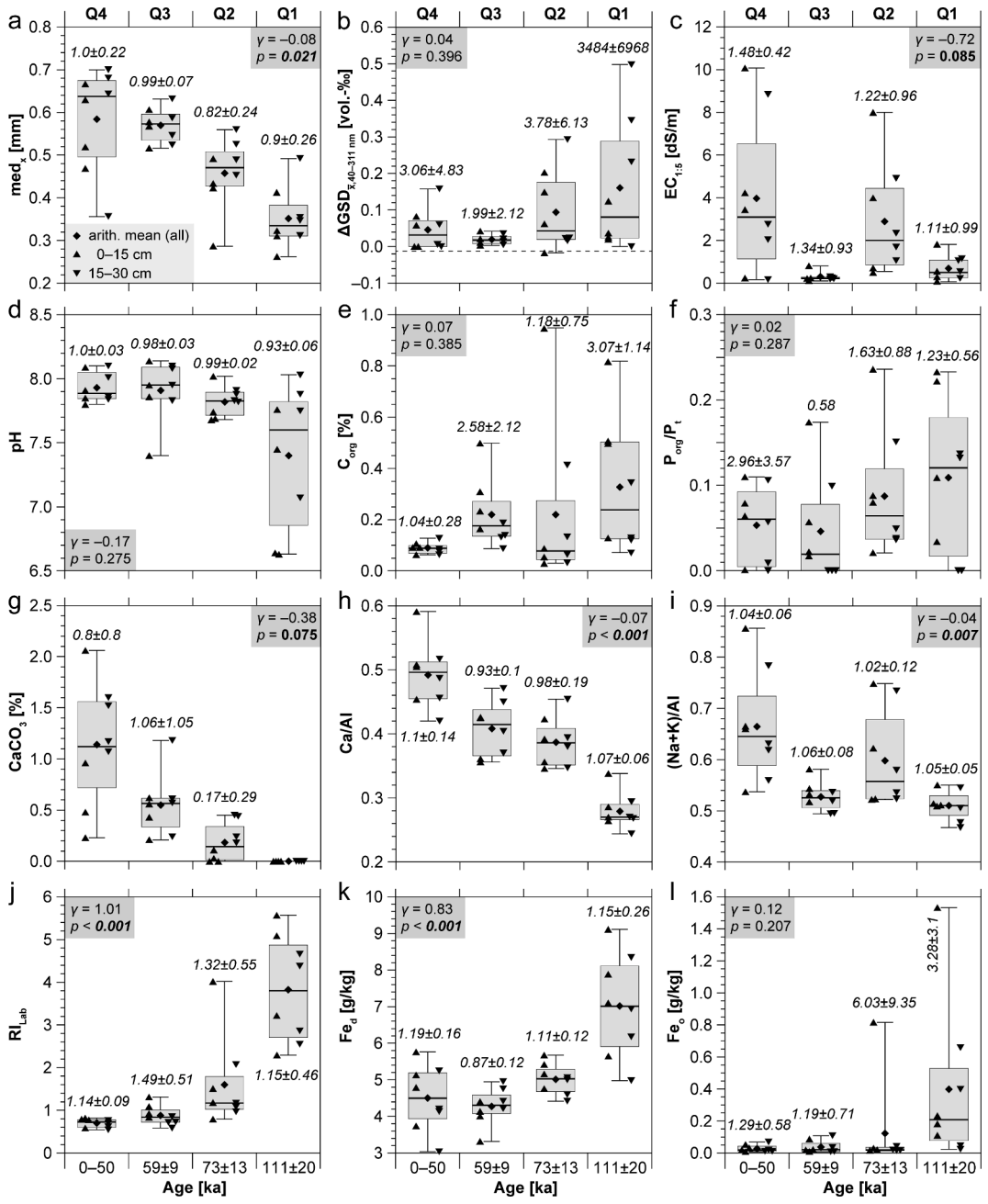

Fig. 6. Boxplot diagrams of physicochemical soil parameters for each morphostratigraphic unit from (left) Q4 to (right) Q1, based on all soil samples analysed per surface generation: (a) med_x = median grain size; (b) $\Delta GSD_{\bar{x},40-311\ nm}$ = differential grain size distribution according to Schulte and Lehmkuhl (2018) for the colloidal grain size fraction between 40 and 311 nm; (c) $EC_{1:5}$ = electrical conductivity in 1:5 soil–water extracts; (d) soil pH; (e) C_{org} = organic C content; (f) P_{org}/P_t = proportion of organic P in total P; (g) $CaCO_3$ content; (h) Ca/Al = decalcification proxy according to Buggle et al. (2011); (i) (Na + K)/Al = salinization proxy after Sheldon and Tabor (2009); (j) RI_{Lab} = redness index after Barrón and Torrent (1986); (k) Fe_d = content of dithionite-soluble pedogenic iron; (l) Fe_o = content of oxalate-soluble pedogenic iron. Plotted are also the individual data categorized by the sample depth interval, and the total arithmetic mean as well as the mean ratio between top- and bottom-soil analyses (numbers in italics ± 1σ) per surface generation. To test if the relative age difference along the chronosequence has significant effects on the pedological results when all samples per generation (n = 8) are considered and the sample depth is accounted for as a random effect, linear mixed models were applied using the residual maximum likelihood criterion (Bates et al., 2015); the slope of the age effect (γ) and the statistical significance (p-value; $\alpha \leq 0.1$ in bold, $\alpha \leq 0.05$ in bold italics) using Satterthwaite's method for t-tests are indicated in the grey boxes. Ages given for the surface generations correspond to the derived total landform ages (± external uncertainties) and morphochronological interpretation (see sections 4.1 and 5.1 for details).

of the Morro Mejillones (Marquardt, 2005; Cortés et al., 2012; Ritz et al., 2019), the only other CAF characterized by four morphostratigraphic units is located further north at Guanillos (~22°S) (Walk et al., 2019, 2022). According to the CAF Guanillos which served to constrain the effects of coastal weathering on the spectral, textural, and gravelometric surface characteristics under distinctive hyperaridity and total absence of vegetation on a Late Quaternary timescale (Walk et al., 2022), we argue that the numerically dated chronosequence across the CAF Paposo provides a unique opportunity to study the processes and evolution of soil formation in a coastal environment at the transition from a hyper-arid to arid climate.

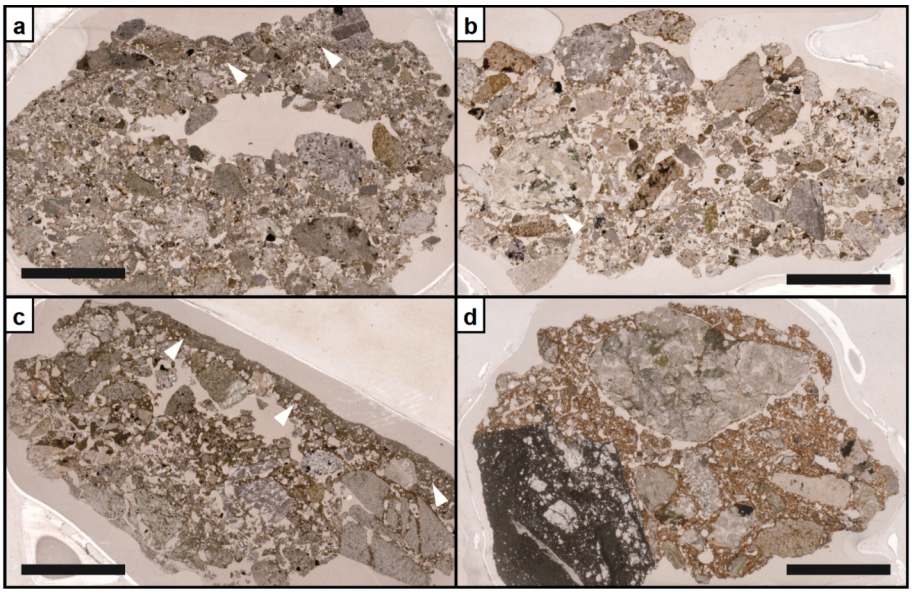

Fig. 7. Thin sections of soil samples taken from (a) Q4 to (d) Q1 as captured under transmitted light using a flatbed scanner: (a) thin section CL22-014 from Q4 (depth: 0–3 cm) showing a mixture of well-rounded gravel with limited amounts of fine particles and a washed-in microlayer of fines near the top (white arrows); (b) thin section CL22-022 from Q3 (depth: 20–25 cm) consisting predominantly of loosely packed gravel and featuring a thin carbonate crust underneath single rock fragments (white arrow); (c) surface sample CL22-017 from Q2 (depth: 0–2 cm) characterized by increased fine material and notably darker, reddish-brown, colour of the groundmass compared to samples from younger fan generations (a, b); note the structural crust at the top (white arrows) indicating the surface of Q2; (d) thin section CL22-013B (depth: 25–30 cm) from Q1 featuring an intensively reddish-brown groundmass. Scale bars are 10 mm.

5.1. *Alluvial fan morphogenesis*

Large scatter is a common observation in exposure age distributions of alluvial fan surfaces due to the nature of the aggradational process superimposed by counteracting effects of pre- and post-depositional modifications (e.g., Dühnforth et al., 2007; Spelz et al., 2008; Owen et al., 2014; Cesta and Ward, 2016; D'Arcy et al., 2019). Pre-depositional exposure due to intermediate deposition and reworking leads to a positively skewed distribution of exposure ages (Saha et al., 2018; D'Arcy et al., 2019). At the CAF Paposo, we consider this effect to be the dominant 'geomorphological uncertainty' determining the choice of a preferred component Gaussian (cf. section 3.1.3), since a positive skewness can be observed in the exposure age distributions – in particular, for Q2 (Supplementary Fig. SF4) – and has also been reported for exposure dating of other alluvial fans at the coast of the Atacama Desert (Bartz et al., 2020a; Walk et al., 2022). Corresponding selection of the youngest component Gaussian is, however, not justifiable solely based on the multimodal age distributions of Q1 and Q3. Instead, we argue that the large catchment, which features poor sediment connectivity in its vast hinterlands (Walk et al., 2020), is prone to transient sediment storage along its drainage network (Fig. 1). This is further supported by the ^{10}Be concentrations of the recent channel sediment (PAP-22) exceeding those of most (17 of 20) analysed samples (Table 2). Due to a textural composition of the channel sediment being much finer than the boulders sampled from the abandoned fan surfaces; however, a potential grain-size bias needs to be taken into account when comparing both sample types. Grain-size bias in ^{10}Be concentrations might be caused by (i) deep-seated erosion processes including landslides and debris flows (Brown et al., 1995; Tofelde et al., 2018; van Dongen et al., 2019) and (ii) differential impact of ^{10}Be inheritance caused by transient storage of the sediment, which largely depends on the responsible transport process; for instance, highly energetic and continuous transport by debris flows versus cascade-like transport of sands and gravels by water flows (Costa, 1988; Blair and McPherson, 2009; Aguilar et al., 2014; 2020; Cabré et al., 2020). Thus, while sample PAP-22 indicates a potentially strong effect of pre-exposure on the ^{10}Be concentrations in aggraded deposits, it cannot be used to correct for the inheritance component in the concentrations of the exposed boulders. In contrast, selection of embedded boulders featuring insignificant signs of weathering and erosion, and a surrounding fan surface morphology largely free of secondary channels, excludes a significant contribution of post-depositional degradation and exhumation, respectively (Fig. 4; Supplementary Fig. SF3 and SF4).

Resulting total landform ages of the preferred component Gaussians are interpreted as ages of terminal aggradation because a fan surface generation is formed by many depositional events over a considerable timespan (e.g., Blair and McPherson, 2009; D'Arcy et al., 2019). As a consequence, a coherent morphochronology of the CAF Paposo could be established that allows for the deduction of its overall morphogenesis (Fig. 8a). While the oldest preserved fan generation Q1 aggraded in orientation with the feeder channel until the early to middle last interglacial period (MIS 5e–c), abandonment is suggested to have occurred latest during the transition from the MIS 5b to 5a, contemporaneously with a lateral shift of the depositional centre and initial formation of Q2. Higher morphodynamic activity of alluvial fans during MIS 5 has been constrained widely along the coast (Bartz et al., 2020a) and related to a higher frequency of precipitation events following a northward shift of the austral mid-latitude westerlies during phases of precession maxima (Lamy et al., 2000; Stuut and Lamy, 2004) as well as warmer SST of the SE Pacific (Fig. 8; Calvo et al., 2001; Rincón-Martínez et al., 2010).

Enhanced aggradation of Q2 occurred during the transition MIS 5 to MIS 4 and might also be linked to a higher pluvial intensity driven by atmospheric changes in the SE Pacific. These are preserved in the marine sedimentary record to the south (Fig. 8; Stuut and Lamy, 2004) but not in terrestrial, fluvial-alluvial archives further north – neither along the coast (Bartz et al., 2020a) nor within the Coastal Cordillera (Ritter et al., 2019).

The abandonment of Q2 by incision and subsequent progradation to form Q3 could chronologically be constrained to the MIS 4 by a weakly significant (1σ) separability between the respective landform ages (Fig. 8a). The morphostratigraphic differentiation might be linked to the aforementioned variability of palaeoprecipitation, to the falling sea level (Fig. 8c), to a phase of increased tectonic uplift, or to autogenic controls (cf. Ventra and Clarke, 2018).

Based on the established morphochronological framework, formation of Q4 cannot be determined more accurately than to have occurred since MIS 3. However, chronological studies by Vargas et al. (2006), Bartz et al. (2020a) and Walk et al. (2022) conducted on alluvial fans along the coastal Atacama indicate prominent geomorphological changes during the Holocene. Preserved in form of the coastal cliff (Fig. 1b), base-level changes by the Holocene sea-level rise and subsequent marine toe cutting can be considered to have affected the CAF Paposo alike. At the CAF Guanillos, incision of the main channel could further be dated to the Early to Mid-Holocene (Walk et al., 2022),

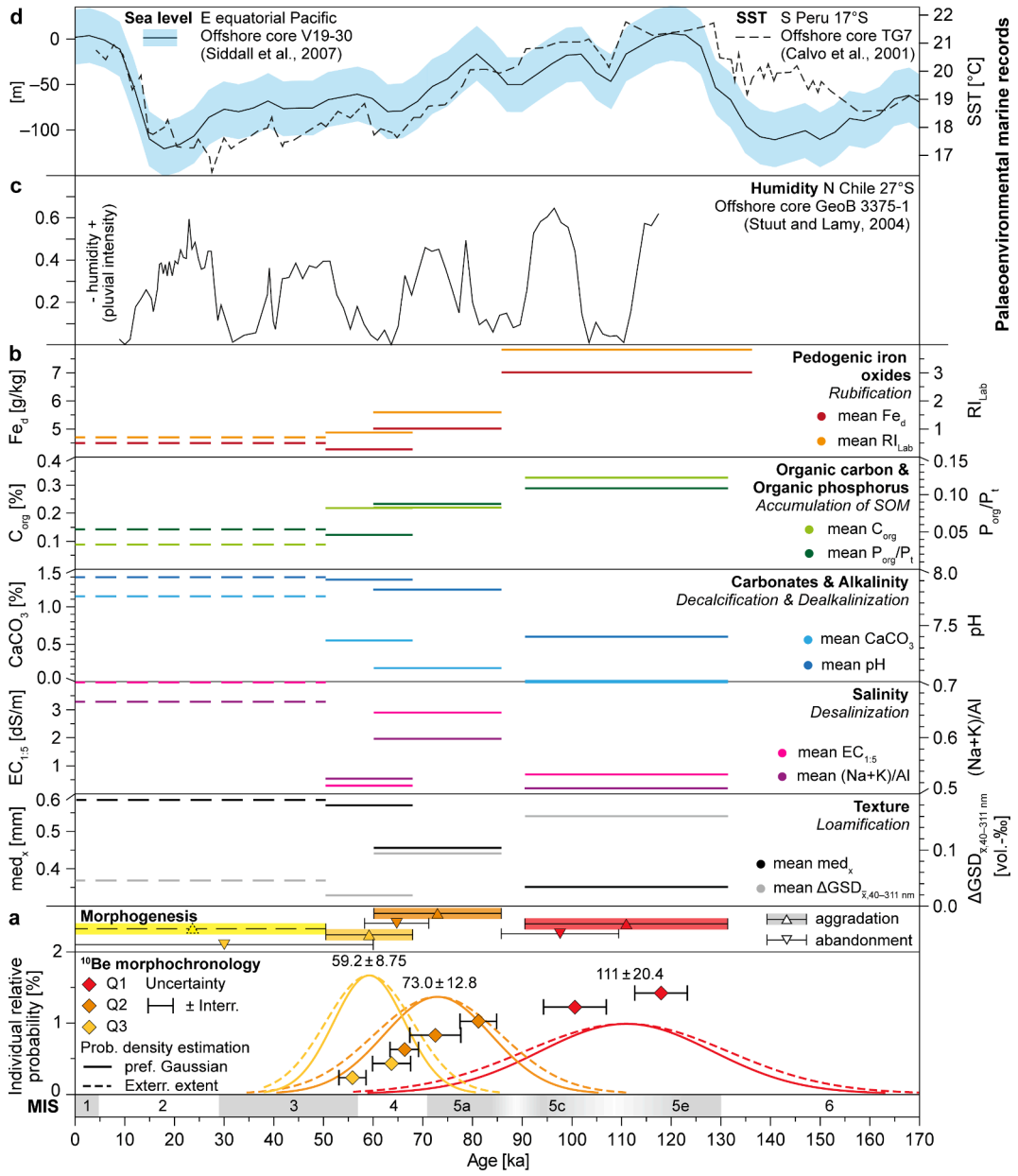

Fig. 8. (a) ^{10}Be exposure-age based morphochronology for the CAF Paposo since the MIS 6, showing the individual preferred component Gaussian PDEs and corresponding external uncertainties, resulting total landform ages (± external uncertainties as well as exposure ages (± internal uncertainties) completely enclosed at 2σ by the preferred component Gaussian (see sections 3.1.3 and 4.2 for details) – all coloured according to the abandoned surface generation (Q3 – light orange, Q2 – orange, Q1 – red); displayed above are deduced timespans for aggradation and abandonment of each generation during the fan's morphogenesis using the same colour code (inferred Q4 – yellow, dashed lines). (b) Physicochemical soil parameters quantifying the texture, salinity, carbonate content and alkalinity, organic carbon and organic phosphorus, and pedogenic iron oxides plotted against absolute ages of morphostratigraphic units (aggradation timespans: continuous lines – dated, dashed lines – inferred) and deduced pedological processes (in italics); texture: (left) median grain size (med_x) and (right) differential grain size distribution according to Schulte and Lehmkuhl (2018) for the colloidal grain size fraction between 40 and 311 nm ($\Delta GSD_{\bar{x},40-311\ nm}$); salinity: (left) electrical conductivity in 1:5 soil–water extracts ($EC_{1:5}$) and (right) salinization proxy (Na + K)/Al after Sheldon and Tabor (2009); carbonates and alkalinity: (left) $CaCO_3$ content and (right) soil pH value; organic carbon and organic phosphorus: (left) organic C content (C_{org}) and (right) proportion of organic P in total P (P_{org}/P_t); pedogenic iron oxides: (left) content of dithionite-soluble pedogenic iron (Fe_d) and (right) redness index after Barrón and Torrent (1986) (RI_{Lab}). Results are further compared to (c) a marine offshore record of N Chilean humidity (pluvial intensity) at 27°S (Stuut and Lamy, 2004), (d, left) sea-level fluctuations after Siddall et al. (2007) based on a benthic isotope record from the E equatorial Pacific (Shackleton and Pisias, 1985), scaled according to Cutler et al. (2003), and (d, right) a marine offshore record of sea surface temperatures (SST) at 17°S (Calvo et al., 2001). Note that in (d) variations in the scaled benthic isotope curve are covered by a ± 30 m envelope. Displayed marine isotope stages (MIS) follow Lisiecki and Raymo (2005). (For interpretation of the references to colour in this figure legend, the reader is referred to the web version of this article.)

contemporaneous with the sea-level maximum as well as the onset of the modern El Niño-Southern Oscillation (Vargas et al., 2006; Siddall et al., 2007). We thus argue that, although the onset of the formation of Q4 might date back to MIS 3, channel beds, sub-recent terraces, and progradation onto the shore developed since the Early Holocene.

5.2. *Late Quaternary pedogenesis at the coastal arid-hyperarid transition*

Along the Late Quaternary chronosequence at the CAF Paposo, physicochemical soil properties, supported by micromorphological evidence, suggest initial but clearly identifiable soil formation expressed in

loamification, decalcification coupled with a dealkalinization, accumulation of SOM, and an increase of pedogenic iron related to either brunification or rubification (Fig. 8b). Soil analyses were conducted only on the upper 30 cm in order to, i.a., minimize the effect of stratigraphic variability of the hyperconcentrated flow and sheet flow deposits on the pedological results. However, this strictly limits the validity of the interpreted pedogenic processes to the upper soil profiles. Those deduced processes all show a consistent, monotonic relation with absolute fan surface exposure age. The largest changes in soil properties have occurred between MIS 5 and the MIS 4/3-transition over a timespan of ~30 to ~60 ka in a roughly linear (pH, C_{org}) to sublinear (med_x, $\Delta GSD_{\bar{x}\,40-311\ nm}$, $CaCO_3$, Fe_d, RI_{Lab}) behaviour (Fig. 8b). In addition, an inconsistent yet significant trend towards desalinization with age became apparent. Apart from $CaCO_3$, C_{org}, and the salinity measures $EC_{1:5}$ and (Na + K)/Al, differences in the state of pedogenesis between Q3 and Q4, which developed throughout the past ~50 to 60 ka, are minor.

Some variability of the pedological results within and between the surface generations might also be related to the heterogeneous source-area lithology and alluvial fan stratigraphy (cf. section 2.1 and 2.3, respectively). Thus, our interpretation needs to be considered carefully and is valid only under the assumption that such heterogeneities are negligible. This assumption is supported, however, by the clear and significant trends with age for the grain size (med_x), $CaCO_3$ content, redness (RI_{Lab}), and Fe_d content (Fig. 6). We argue that mostly the igneuous lithology of the downstream and middle reaches are relevant for feeding the CAF Paposo during the Late Quaternary, as it has been shown that sediment connectivity of the large catchments draining the Coastal Cordillera to the coast drastically decreases towards the hinterlands (Walk et al., 2020).

Under consideration of the recent climate in the transition from hyperaridity to aridity, the pedological results are unexpected. Typical features of soils formed under hyperaridity are mostly related to secondary accumulation of salts in horizons characterized depending on the dominant salt as calcic, gypsic, duric, or salic (Nettleton and Peterson, 1983; Ewing et al., 2006; Finstad et al., 2014; IUSS Working Group WRB, 2022). Also along an arid-hyperarid coast in the United Arabic Emirates, Abdelfattah (2013) found that (i) Aridisols formed on alluvial fans, dune sands or along the supratidal shore feature elevated $CaCO_3$ contents mostly exceeding 30% throughout the entire profiles; (ii) pedogenic accumulation of gypsum in the top soils for those pedons developed in coastal dune sand and at the supratidal beach; while (iii) moderate to strong salinity is restricted to the near-shore Aquisalids and Haplosalids. In contrast to those as well as the hyperarid soils in the central Atacama Desert that are formed over much longer timescales than at the coast – on surfaces which date back between the Middle Pleistocene to the Oligocene (e.g., Dunai et al., 2005; Placzek et al., 2010; Baker et al., 2013; Ritter et al., 2018) – leaching of soluble minerals, i.e. $CaCO_3$ and NaCl, prevails in the south-central coastal Atacama since the last interglacial period (Fig. 6; Fig. 8b). Total decalcification of at least the top 30 cm of soils on Q1 and consistent top–bottom ratios in all four profiles on Q2 are a clear indicator for precipitation-induced percolation being responsible for redistribution of salts (Fig. 6g). The age-dependent depletion and downward mobilization of $CaCO_3$ is further supported by the micromorphological findings (Fig. 7). A concomitant concentration of salts in the subsoils can be expected under arid to hyperarid conditions; however, as sampling was restricted to the upper 30 cm, it cannot be assessed in which depth the mobilized salts precipitate.

Atmospheric deposition of sea salt and marine aerosols in combination with local aeolian reworking of mineral fines is found to be the predominant source of soluble minerals at the coast (Rech et al., 2003; Wang et al., 2014). Wang et al. (2014) assessed a deposition rate of soluble salts of 4 kg m^{-2} ka^{-1} under recent coastal conditions, which is over a third higher than in the central Atacama Desert. Decalcification and desalinization constrained along the chronosequence, thus, indicates that the leaching of salts dominates over atmospheric deposition under the fluctuating palaeohumidity integrated over the Late Quaternary (Fig. 8). In turn, initial contents of both $CaCO_3$ and NaCl in the alluvial parent material thus seem to be governed by long-term atmospheric deposition in the higher catchment – given the lack of a carbonatic source-area lithology (Fig. 1a; Escribano et al., 2013; Álvarez et al., 2016). Almost total absence of highly soluble NaCl on Q3, causing a prominent inconsistency in the chronosequence (Fig. 6e, g), might be related to the formation of the original fan surface by erosion (cf. section 2.3) but cannot be certainly explained thereby. Apart from the atmospheric contribution of salts, also aeolian influx of silicate dust is recognized as a major process affecting soil formation; in particular, in arid regions (e.g., Wells et al., 1990; Reheis et al., 1995; Ewing et al., 2006; McAuliffe et al., 2018). Depositon rates of insoluble silicate particles at the coastal Atacama exceed those of salts by a factor of three and can be related to aeolian redistribution or to local anthropogenic dust sources (Wang et al., 2014). Consequently, age-dependent cumulative silicate dust deposition has to be accounted for as a significant process superimposing the deduced *in situ* pedogenesis.

Soil pH values are well buffered as long as $CaCO_3$ is available (Fig. 6d, g; cf. van Breemen et al., 1983). A drop to near-neutral conditions can only be found in completely decalcified soils (Fig. 6d, g). Since acidic soil conditions do not develop on the CAF Paposo over ~90 to ~120 ka, we refer to the respective pedogenic process as dealkalinization instead of acidification (Fig. 8b; cf. Reiniger and Bolt, 1972; van Asten et al., 2004). Sources of H^+ are weathering of minerals, atmospheric CO_2 dissolution, humification, and biotic activity (Fuentes et al., 2022b) but also frequent wetting by acidic coastal fog (Sträter et al., 2010). As the elevation of the advective fog is linked to the sea level as well as SST, the effect of the fog on the alluvial fans at the coastal plain was likely higher during phases of lower sea level largely contemporaneous with colder SST of the SE Pacific (Fig. 8d; Walk et al., 2022). Soil analyses by Fuentes et al. (2022b) along a catena from ~100 to ~700 m a.s.l. at the southern Morro Moreno National Park (23.52°S/70.56°W; Fig. 1a) revealed altitudinal trends of physicochemical, mineralogical, and microbiological properties, which can be related to the elevation-dependent occurrence frequency of fog. It is noteworthy that the pH values, electrical conductivity, as well as contents of C_{org} and P_{org} assessed at the lowermost sample point on a single-phase alluvial fan (T1, Fuentes et al., 2022b) are in good agreement with our results obtained for Q4 at Paposo (Table 3; Fig. 6).

We thus argue that the advective fog alone does not explain the processes and intensity of soil formation assessed across the CAF. In addition, sufficient precipitation is required to cause, i.a., the observed leaching of soluble constituents. This is confirmed by the soil water content in 10 cm depth monitored at a nearby meteorological station located below the lower boundary of advective fog, at 160 m a.s.l. (Supplementary Fig. SF2; Hoffmeister, 2018). Soil water contents >10% that allow for percolation in soils with a sandy texture are reached only after precipitation events of ≥3 mm and occur under current climatic conditions several times per year (Supplementary Fig. SF2). Note that percolation in the loamy soils of Q1 tends to require a higher soil moisture (cf. Blum, 2012). Precipitation with a significantly higher intensity than drizzle was likely more frequent at the south-central coast of the Atacama during phases of the MIS 5, transition to MIS 4, MIS 3, and, in particular, during the LGM (Fig. 8c; cf. sections 2.2 and 5.1; Stuut and Lamy, 2004).

Given the abandoned CAF generations did not experience major reworking or erosion for at least some thousand years, C_{org} contents in the order of several g/kg are equivalent to those assessed by Mörchen et al. (2019) in the lower reaches of the Paposo catchment up to elevations of 900 m a.s.l. (cf. Fig. 1a; Table 3). In this altitudinal belt of highest fog occurrence, the biomarker signatures of the fog-fed Loma vegetation and soils differ strongly from those affected by rain in the central to eastern Atacama Desert (Mörchen et al., 2021). Furthermore, it is suggested that the high variability of C_{org} contents on each abandoned fan generation (Fig. 6e) results from the small-scale distribution

pattern of recent and past plant growth (cf. Mörchen et al., 2019; Fuentes et al., 2022b). As an essential nutrient for plants, phosphate is transformed to organic P compounds and incorporated in the soil as plant detritus (Fuentes et al., 2022b). Ca-phosphates have been found to be the primary retention form of P in the soils in the middle reaches of the Paposo Valley (Moradi et al., 2020). In accordance with the results of Fuentes et al. (2022b), we can relate the increasing P_{org}/P_t ratio predominantly to a long-term decline in the limited stock of P_{inorg} concomitant with the age-dependent cumulative effect of plant growth reflected in the C_{org} contents (Fig. 8b). Accumulation of SOM is further associated with the occurrence of biogenic chambers, burrows and channels; that are signs of bioturbation (Fig. 7). Moreover, dealkalinization might be fostered to some degree by humification of organic plant residues to humic acids over a Late Quaternary timescale (e.g., van Breemen et al., 1983; Thomas and Hargrove; 1984; Fuentes et al., 2022b). Further studies are required though to verify this interrelation and to determine the types of humic substances present under coastal (hyper)aridity.

Relevant constituents in the studied soil which govern the soil colour are mostly SOM, carbonates, and iron oxide minerals. While the contents of C_{org} and $CaCO_3$ have opposing effects on the luminance (L*), pedogenic iron oxides (Fe_d) correlate positively with the redness (RI_{Lab}) of the soils and age of the CAF chronosequence (Fig. 7; Fig. 8b). Fe_d was, for instance, also used by Harvey et al. (2003) to successfully differentiate a Quaternary alluvial fan sequence in arid SE Spain and, likewise, a positive relation with relative age was ascertained. However, Fe_d alone does not allow for deducing the dominant pedogenic iron oxide being formed (Mehra and Jackson, 1958; Schwertmann, 1959). In light of this, Barrón and Torrent (1986) showed that the RI_{Lab} is especially sensitive to hematite and can be used to quantitatively estimate its content; yet distinguishing a potential contribution by goethite is not trivial (cf. Sahwan et al., 2021). Although goethite is reported to be abundant also in desert soils (Lafon et al., 2004), frequent wetting and drying cycles at the south-central coastal Atacama Desert (Supplementary Fig. SF2), in combination with slightly alkaline to near-neutral soil conditions, are favourable for the formation of hematite (Schwertmann and Murad, 1983; Bertrams et al., 2014). A predominant formation of pedogenic hematite is corroborated by comparing the interrelation of the samples' CIELAB chromacity coordinates a* and b* with relative age to the colorimetric development during crystallization from ferrihydrite to either goethite or hematite, studied experimentally by Nagano et al. (1994) (Supplementary Fig. SF5). We refer to the pedogenic hematite formation as rubification, following the definition of Schwertmann et al. (1983), and which is typical under (sub-)tropical and Mediterranean climates characterized by strong seasonality of humidity (Gardner and Pye, 1981). In contrast, brunification is driven by the formation of clay-iron-humus complexes in acidic soils, generally occurs in humid and temperate climates (Duchaufour and Souchier, 1978), and thus involves a considerable accumulation of goethite (e.g., Fedoroff, 1997; Wagner et al., 2014). Although argued to have resulted primarily from *in situ* formation of pedogenic hematite, also aeolian input might have contributed to the accumulation of Fe_d, as it has been recently shown that the dithionite-citrate-bicarbonate treatment does not reliably separate pedogenic from aeolian iron oxides (Yang et al., 2022).

Most of the assessed pedogenic processes jointly affect the texture of the soils, which all contain large to predominant proportions of clasts in the gravel or cobble fraction (cf. section 2.3; Fig. 7), yet are developed in a finer matrix showing a significant fining trend with age (Fig. 5; Fig. 6a). Over a Late Quaternary timescale, loamification leads to finer textural compositions classified for the majority of soil samples from Q1 as (coarse) sandy loam (Table 3; Fig. 8b). Loamification results from the post-depositional formation of soil constituents summarized under colloids (cf. Molina, 2013) but can further be superimposed by post-depositional weathering of coarser grains, reworking of particles by runoff (de Haas et al., 2014; Walk et al., 2022), as well as atmospheric deposition of dust (Arenas-Díaz et al., 2022). Relevant secondarily formed colloids comprise pedogenic iron oxides, clay minerals, and humic substances (Molina, 2013; Moradi et al., 2020). The slight and variable increase of both the clay content as well as $\Delta GSD_{\bar{x},40-311\ nm}$ along the chronosequence indicates that loamification is in an initial stage (Fig. 5; Fig. 6b). Furthermore, the studied soils are affected by lateral and vertical relocation of fines following significant rainfall (Fig. 7; cf. Williams et al., 2018). It has been stressed, however, that decalcification is necessary to allow for translocation of clay involved in advanced loamification (Hirsch et al., 2021). Hence, this potentially affects the soils under coastal (hyper)aridity only over a timeframe longer than ~90 ka (Q1). In addition, clast breakdown especially by salt weathering but to a minor degree also by insolation weathering and the formation of weathering rinds need to be considered, as those processes have been shown to govern the surficial grain size distribution of the CAF of the Atacama Desert (Walk et al., 2022) and were detected also in the studied soils (Fig. 7c). However, in contrast to the coastal environment further north, salt weathering seems to be of much lesser importance since (palaeo)precipitation throughout the Late Quaternary has been sufficiently high to counterbalance the accumulation of salts by atmospheric deposition (Fig. 8b). As the soil texture, in turn, strongly impacts the soil water storage and mobility, we infer that loamification has an impeding effect on the leaching of salts as well as the translocation of insoluble minerals on timescales larger than 10^5 a.

6. Conclusion

The processes and timescales of pedogenesis assessed along a Late Quaternary soil chronosequence that developed under a coastal climate in the arid-hyperarid transition of the western south-central Atacama Desert strongly differ from those characteristics found for Aridisols in inland deserts. Using ^{10}Be cosmogenic nuclide exposure dating, terminal aggradation of three abandoned alluvial fan surface generations was constrained to 111 ± 20.4 ka, 73.0 ± 12.8 ka, and 59.2 ± 8.75 ka for Q1, Q2, and Q3, respectively, and followed by the incision of the active main channel (Q4) likely since the Early Holocene. Along this chronosequence, restricted to the upper 30 cm of coastal soils and located below the zone directly affected by frequent fog occurrence, physicochemical soil properties show negative relations with growing age for the median grain size, salinity, long-term pH development, and $CaCO_3$ contents, while organic carbon, the ratio of organic to total phosphorus, the redness, and the contents of total and poorly crystalline pedogenic iron oxides tend to increase with age. The degree of pedogenic alteration can be attributed to the cumulative precipitation received since terminal aggradation, though the largest pedological changes evolved (sub)linearly over a timespan of ~30 to ~60 ka between the MIS 5 and MIS 4/3-transition and might be linked to periods of higher pluvial intensity driven by atmospheric changes in the SE Pacific. Further supported by micromorphological findings, we conclude the following soil forming processes prevail over a Late Quaternary timescale:

- Redistribution of soluble salts by leaching causing long-term desalinization and depletion of $CaCO_3$ towards total decalcification that further provokes dealkalinization in the upper soils
- Accumulation of SOM, reflected in increasing contents of C_{org} and proportions of P_{org}, signs of bioturbation, and characterized by a high spatial variability depending on the small-scale distribution pattern of plant growth
- Initial rubification following the formation of pedogenic iron oxides; in particular, hematite, causing a reddening of the soils
- Initial loamification primarily driven by long-term accumulation of colloidal iron oxides, clay minerals, and humic substances

In addition, atmospheric influx of insoluble dust particles – supposedly originating mostly from local aeolian redistribution – has to be accounted for to considerably affect soil formation. Although further studies are required to assess the relevance of aeolian influx in relation

to *in situ* processes, our results contribute to a better understanding of pedogenesis at arid to hyperarid coasts occurring widely spread across the Earth (Feng and Fu, 2013; Trabucco and Zomer, 2019). As soils are crucial components of coastal ecosystems, which further constitute centres of population especially in arid regions (Martínez et al., 2007), the pedogenic processes and related timescales assessed at the south-central coast of the Atacama Desert have global implications.

CRediT authorship contribution statement

Janek Walk: Conceptualization, Methodology, Investigation, Writing – original draft, Visualization, Data curation. **Philipp Schulte:** Methodology, Investigation, Validation, Writing – review & editing. **Melanie Bartz:** Investigation, Writing – review & editing. **Ariane Binnie:** Investigation, Writing – review & editing. **Martin Kehl:** Investigation, Visualization, Writing – original draft. **Ramona Mörchen:** Investigation, Writing – original draft. **Xiaolei Sun:** Conceptualization, Writing – review & editing. **Georg Stauch:** Writing – review & editing, Supervision. **Christopher Tittmann:** Investigation. **Roland Bol:** Conceptualization. **Helmut Brückner:** Project administration, Funding acquisition, Conceptualization, Writing – review & editing. **Frank Lehmkuhl:** Supervision, Resources, Project administration, Funding acquisition, Writing – review & editing.

Declaration of Competing Interest

The authors declare that they have no known competing financial interests or personal relationships that could have appeared to influence the work reported in this paper.

Data availability

Results of the grain size determination and further physicochemical soil parameters can be accessed under doi: 10.5880/CRC1211DB.55 and doi: 10.5880/CRC1211DB.56, respectively. Pedological research data is made available at the CRC1211 database. The geochronological data created within the study is included in the publication.

Acknowledgements

This project is funded by the Deutsche Forschungsgemeinschaft (DFG, German Research Foundation) as part of the CRC 1211 'Earth – Evolution at the Dry Limit' (subproject C2) under Grant 268236062 – SFB 1211. We are grateful to E. Campos from the Universidad Católica del Norte in Antofagasta for his assistance in organization of the field campaigns. M. Keiser is thanked for his help during field work in 2018 and we gratefully acknowledge the laboratory assistance by E. Voronina, M. Dohms, R. Erdweg, and K. Jung. Furthermore, we thank two anonymous reviewers for their constructive comments on the manuscript.

Appendix A. Supplementary material

Supplementary data to this article can be found online at https://doi.org/10.1016/j.catena.2023.107171.

References

Abdelfattah, M.A., 2013. Pedogenesis, land management and soil classification in hyper-arid environments: results and implications from a case study in the United Arab Emirates. Soil Use Manag. 29, 279–294. https://doi.org/10.1111/sum.12031.

Aguilar, G., Carretier, S., Regard, V., Vassallo, R., Riquelme, R., Martinod, J., 2014. Grain size-dependent ^{10}Be concentrations in alluvial stream sediment of the Huasco Valley, a semi-arid Andes region. Quat. Geochronol. 19, 163–172. https://doi.org/10.1016/j.quageo.2013.01.011.

Aguilar, G., Cabré, A., Fredes, V., Villela, B., 2020. Erosion after an extreme storm event in an arid fluvial system of the southern Atacama Desert: an assessment of the magnitude, return time, and conditioning factors of erosion and debris flow generation. Nat. Hazards Earth Syst. Sci. 20, 1247–1265. https://doi.org/10.5194/nhess-20-1247-2020.

Allmendinger, R.W., González, G., 2010. Invited review paper: Neogene to Quaternary tectonics of the coastal Cordillera, northern Chile. Tectonophysics 495, 93–110. https://doi.org/10.1016/j.tecto.2009.04.019.

Álvarez, J., Jorquera, R., Miralles, C., Padel, M., Martínez, P., 2016. Cartas Punta Posallaves y Sierra Vicuña Mackenna, Región de Antofagasta, Serie Geología Básica 183-184, 147 p., 1 mapa escala 1:100.000. Servicio Nacional de Geología y Minería, Santiago.

Amundson, R., Dietrich, W., Bellugi, D., Ewing, S., Nishiizumi, K., Chong, G., Owen, J., Finkel, R., Heimsath, A., Stewart, B., Caffee, M., 2012. Geomorphologic evidence for the late Pliocene onset of hyperaridity in the Atacama Desert. GSA Bull. 124, 1048–1070. https://doi.org/10.1130/B30445.1.

Arenas-Díaz, F., Fuentes, B., Reyers, M., Fiedler, S., Böhm, C., Campos, E., Shao, Y., Bol, R., 2022. Dust and aerosols in the Atacama Desert. Earth Sci. Rev. 226, 103925 https://doi.org/10.1016/j.earscirev.2022.103925.

Arens, F.L., Airo, A., Feige, J., Sager, C., Wiechert, U., Schulze-Makuch, D., 2021. Geochemical proxies for water-soil interactions in the hyperarid Atacama Desert. Chile. Catena 206, 105531. https://doi.org/10.1016/j.catena.2021.105531.

Azua-Bustos, A., González-Silva, C., Mancilla, R.A., Salas, L., Gómez-Silva, B., McKay, C. P., Vicuña, R., 2011. Hypolithic cyanobacteria supported mainly by fog in the coastal range of the Atacama Desert. Microb. Ecol. 61, 568–581. https://doi.org/10.1007/s00248-010-9784-5.

Azua-Bustos, A., Urrejola, C., Vicuña, R., 2012. Life at the dry edge: Microorganisms of the Atacama Desert. FEBS Lett. 586, 2939–2945. https://doi.org/10.1016/j.febslet.2012.07.025.

Azua-Bustos, A., Caro-Lara, L., Vicuña, R., 2015. Discovery and microbial content of the driest site of the hyperarid Atacama Desert, Chile. Environ. Microbiol. Rep. 7, 388–394. https://doi.org/10.1111/1758-2229.12261.

Baker, A., Allmendinger, R.W., Owen, L.A., Rech, J.A., 2013. Permanent deformation caused by subduction earthquakes in northern Chile. Nat. Geosci. 6, 492–496. https://doi.org/10.1038/ngeo1789.

Balco, G., Stone, J.O., Lifton, N.A., Dunai, T.J., 2008. A complete and easily accessible means of calculating surface exposure ages or erosion rates from ^{10}Be and ^{26}Al measurements. Quat. Geochronol. 3, 174–195. https://doi.org/10.1016/j.quageo.2007.12.001.

Barrón, V., Torrent, J., 1986. Use of the Kubelka-Munk theory to study the influence of iron oxides on soil colour. J. Soil Sci. 37, 499–510. https://doi.org/10.1111/j.1365-2389.1986.tb00382.x.

Bartz, M., Duval, M., Brill, D., Zander, A., King, G.E., Rhein, A., Walk, J., Stauch, G., Lehmkuhl, F., Brückner, H., 2020a. Testing the potential of K-feldspar pIR-IRSL and quartz ESR for dating coastal alluvial fan complexes in arid environments. Quat. Int. 556, 124–143. https://doi.org/10.1016/j.quaint.2020.03.037.

Bartz, M., Walk, J., Binnie, S.A., Brill, D., Stauch, G., Lehmkuhl, F., Hoffmeister, D., Brückner, H., 2020b. Late Pleistocene alluvial fan evolution along the coastal Atacama Desert (N Chile). Global Planet. Change 190, 103091. https://doi.org/10.1016/j.gloplacha.2019.103091.

Bates, D., Mächler, M., Bolker, B.M., Walker, S.C., 2015. Fitting linear mixed-effects models using lme4. J. Stat. Softw. 67, 1–48. https://doi.org/10.18637/jss.v067.i01.

Bertrams, M., Protze, J., Eckmeier, E., Lehmkuhl, F., 2014. A geochemical approach on reconstructing Upper Pleistocene environmental conditions from wadi deposits – an example from the Wadi Sabra (Jordan). Zeitschrift für Geomorphologie, Supplementary Issues 58, 51–80. https://doi.org/10.1127/0372-8854/2013/S-00156.

Binnie, S.A., Dunai, T.J., Voronina, E., Goral, T., Heinze, S., Dewald, A., 2015. Separation of Be and Al for AMS using single-step column chromatography. Nucl. Instrum. Methods Phys. Res., Sect. B 361, 397–401. https://doi.org/10.1016/j.nimb.2015.03.069.

Binnie, S.A., Dewald, A., Heinze, S., Voronina, E., Hein, A., Wittmann, H., von Blanckenburg, F., Hetzel, R., Christl, M., Schaller, M., Léanni, L., ASTER Team, Hippe, K., Vockenhuber, C., Ivy-Ochs, S., Maden, C., Fülöp, R.H., Fink, D., Wilcken, K.M., Fujioka, T., Fabel, D., Freeman, S.P.H.T., Xu, S., Fifield, L.K., Akçar, N., Spiegel, C., Dunai, T.J., 2019. Preliminary results of CoQtz-N: A quartz reference material for terrestrial in-situ cosmogenic ^{10}Be and ^{26}Al measurements. Nuclear Instruments and Methods in Physics Research, Section B: Beam Interactions with Materials and Atoms 456, 203–212. Doi:10.1016/j.nimb.2019.04.073.

Blair, T.C., McPherson, J.G., 2009. Processes and forms of alluvial fans. In: Parsons, A.J., Abrahams, A.D. (Eds.), Geomorphology of Desert Environments, 2nd ed. Springer, Dordrecht, pp. 413–467.

Blum, W.E.H., 2012. Bodenkunde in Stichworten, 7th ed. Borntraeger, Berlin, Stuttgart.

Bockheim, J.G., Gennadiyev, A.N., Hartemink, A.E., Brevik, E.C., 2014. Soil-forming factors and *Soil Taxonomy*. Geoderma 226–227, 231–237. https://doi.org/10.1016/j.geoderma.2014.02.016.

Borchers, B., Marrero, S., Balco, G., Caffee, M., Goehring, B., Lifton, N., Nishiizumi, K., Phillips, F., Schaefer, J., Stone, J., 2016. Geological calibration of spallation production rates in the CRONUS-Earth project. Quat. Geochronol. 31, 188–198. https://doi.org/10.1016/j.quageo.2015.01.009.

Bozkurt, D., Rondanelli, R., Garreaud, R.D., Arriagada, A., 2016. Impact of warmer eastern tropical Pacific SST on the March 2015 Atacama floods. Mon. Weather Rev. 144, 4441–4460. https://doi.org/10.1175/MWR-D-16-0041.1.

British Oceanographic Data Centre (BODC), 2014. The GEBCO_2014 Grid, version 20150318. British Oceanographic Data Centre, Liverpool, UK. URL: https://www.gebco.net/ (Accessed 27 December 2022).

Brown, E.T., Stallard, R.F., Larsen, M.C., Raisbeck, G.M., Yiou, F., 1995. Denudation rates determined from the accumulation of in situ-produced ^{10}Be in the luquillo

experimental forest, Puerto Rico. Earth Planet. Sci. Lett. 129, 193–202. https://doi.org/10.1016/0012-821X(94)00249-X.
Buggle, B., Glaser, B., Hambach, U., Gerasimenko, N., Markovic, S., 2011. An evaluation of geochemical weathering indices in loess–paleosol studies. Quat. Int. 240, 12–21. https://doi.org/10.1016/j.quaint.2010.07.019.
Cabré, A., Aguilar, G., Mather, A.E., Fredes, V., Riquelme, R., 2020. Tributary-junction alluvial fan response to an ENSO rainfall event in the El Huasco watershed, northern Chile. Progress in Physical Geography: Earth and Environment 44, 1–21. https://doi.org/10.1177/0309133319898994.
Cáceres, L., Gómez-Silva, B., Garró, X., Rodríguez, V., Monardes, V., McKay, C.P., 2007. Relative humidity patterns and fog water precipitation in the Atacama Desert and biological implications. J. Geophys. Res. 112, G04S14. https://doi.org/10.1029/2006JG000344.
Calvo, E., Pelejero, C., Herguera, J.C., Palanques, A., Grimalt, J.O., 2001. Insolation dependence of the southeastern Subtropical Pacific sea surface temperature over the last 400 kyrs. Geophys. Res. Lett. 28, 2481–2484. https://doi.org/10.1029/2000GL012024.
Cereceda, P., Osses, P., Larrain, H., Farías, M., Lagos, M., Pinto, R., Schemenauer, R.S., 2002. Advective, orographic and radiation fog in the Tarapacá region, Chile. Atmospheric Research 64, 261–271. Doi:10.1016/S0169-8095(02)00097-2.
Cereceda, P., Larrain, H., Osses, P., Farías, M., Egaña, I., 2008. The climate of the coast and fog zone in the Tarapacá Region, Atacama Desert, Chile. Atmos. Res. 87, 301–311. https://doi.org/10.1016/j.atmosres.2007.11.011.
Cesta, J.M., Ward, D.J., 2016. Timing and nature of alluvial fan development along the Chajnantor Plateau, northern Chile. Geomorphology 273, 412–427. https://doi.org/10.1016/j.geomorph.2016.09.003.
Coira, B., Davidson, J., Mpodozis, C., Ramos, V., 1982. Tectonic and magmatic evolution of the Andes of northern Argentina and Chile. Earth Sci. Rev. 18, 303–332. https://doi.org/10.1016/0012-8252(82)90042-3.
Cortés, J.A., González, G.L., Binnie, S.A., Robinson, R., Freeman, S.P.H.T., Vargas, G.E., 2012. Paleoseismology of the Mejillones Fault, northern Chile: Insights from cosmogenic ^{10}Be and optically stimulated luminescence determinations. Tectonics 31, TC2017. https://doi.org/10.1029/2011TC002877.
Costa, J.E., 1988. Rheologic, geomorphic and sedimentologic differentiation of water floods, hyperconcentrated flows and debris flows. In: Baker, V.R., Kochel, R.C., Patton, P.C. (Eds.), Flood Geomorphology. Wiley, New York, pp. 113–122.
Creixell, C., Oliveros, V., Vásquez, P., Navarro, J., Vallejos, D., Valin, X., Godoy, E., Ducea, M.N., 2016. Geodynamics of Late Carboniferous-Early Permian forearc in north Chile (28°30′–29°30′S). J. Geol. Soc. London 173, 757–772. https://doi.org/10.1144/jgs2016-010.
Cutler, K.B., Edwards, R.L., Taylor, F.W., Cheng, H., Adkins, J., Gallup, C.D., Cutler, P.M., Burr, G.S., Bloom, A.L., 2003. Rapid sea-level fall and deep-ocean temperature change since the last interglacial period. Earth Planet. Sci. Lett. 206, 253–271. https://doi.org/10.1016/S0012-821X(02)01107-X.
D'Arcy, M.K., Schildgen, T.F., Turowski, J.M., DiNezio, P., 2019. Inferring the timing of abandonment of aggraded alluvial surfaces dated with cosmogenic nuclides. Earth Surf. Dyn. 7, 755–771. https://doi.org/10.5194/esurf-2019-21.
de Haas, T., Ventra, D., Carbonneau, P.E., Kleinhans, M.G., 2014. Debris-flow dominance of alluvial fans masked by runoff reworking and weathering. Geomorphology 217, 165–181. https://doi.org/10.1016/j.geomorph.2014.04.028.
Dewald, A., Heinze, S., Jolie, J., Zilges, A., Dunai, T., Rethemeyer, J., Melles, M., Staubwasser, M., Kuczewski, B., Richter, J., Radtke, U., Von Blanckenburg, F., Klein, M., 2013. CologneAMS, a dedicated center for accelerator mass spectrometry in Germany. Nucl. Instrum. Methods Phys. Res., Sect. B 294, 18–23. https://doi.org/10.1016/j.nimb.2012.04.030.
DIN EN ISO 6878, 2004. Water quality - Determination of phosphorus - Ammonium molybdate spectrometric method.
DIN ISO 11277, 2002. Soil Quality - Determination of particle size distribution in mineral soil material - Method by sieving and sedimentation.
DIN 19539, 2016. Investigation of solids - Temperature-dependent differentiation of total carbon (TOC_{400}, ROC, TIC_{900}).
Dortch, J.M., Tomkins, M.D., Saha, S., Murari, M.K., Schoenbohm, L.M., Curl, D., 2022. A tool for the ages: The Probabilistic Cosmogenic Age Analysis Tool (P-CAAT). Quat. Geochronol. 71, 101323 https://doi.org/10.1016/j.quageo.2022.101323.
Duchaufour, P., Souchier, B., 1978. Roles of iron and clay in genesis of acid soils under a humid, temperate climate. Geoderma 20, 15–26. https://doi.org/10.1016/0016-7061(78)90046-0.
Dühnforth, M., Densmore, A.L., Ivy-Ochs, S., Allen, P.A., Kubik, P.W., 2007. Timing and patterns of debris-flow deposition on Shepherd and Symmes creek fans, Owens Valley, California, deduced from cosmogenic ^{10}Be. Journal of Geophysical Research: Earth Surface 112, F03S15. Doi:10.1029/2006JF000562.
Dunai, T.J., González López, G.A., Juez-Larré, J., 2005. Oligocene-Miocene age of aridity in the Atacama Desert revealed by exposure dating of erosion-sensitive landforms. Geology 33, 321–324. https://doi.org/10.1130/G21184.1.
Eckmeier, E., Egli, M., Schmidt, M.W.I., Schlumpf, N., Nötzli, M., Minikus-Stary, N., Hagedorn, F., 2010. Preservation of fire-derived carbon compounds and sorptive stabilisation promote the accumulation of organic matter in black soils of the Southern Alps. Geoderma 159, 147–155. https://doi.org/10.1016/j.geoderma.2010.07.006.
Escribano, J., Martínez, P., Domagala, J., Padel, M., Espinoza, M., Jorquera, R., Contreras, J.P., De La Cruz, R., Calderón, M., 2013. Cartas Bahía Isla Blanca y Taltal, Región de Antofagasta, Serie Geología Básica 164-165, 75 p., 1 mapa escala 1: 100.000. Servicio Nacional de Geología y Minería, Santiago.
Ewing, S.A., Sutter, B., Owen, J., Nishiizumi, K., Sharp, W., Cliff, S.S., Perry, K., Dietrich, W., McKay, C.P., Amundson, R., 2006. A threshold in soil formation at Earth's arid–hyperarid transition. Geochim. Cosmochim. Acta 70, 5293–5322. https://doi.org/10.1016/j.gca.2006.08.020.
Ewing, S.A., Yang, W., DePaolo, D.J., Michalski, G., Kendall, C., Stewart, B.W., Thiemens, M., Amundson, R., 2008. Non-biological fractionation of stable Ca isotopes in soils of the Atacama Desert, Chile. Geochim. Cosmochim. Acta 72, 1096–1110. https://doi.org/10.1016/j.gca.2007.10.029.
Fedoroff, N., 1997. Clay illuviation in Red Mediterranean soils. Catena 28, 171–189. https://doi.org/10.1016/S0341-8162(96)00036-7.
Feng, S., Fu, Q., 2013. Expansion of global drylands under a warming climate. Atmos. Chem. Phys. 13, 10081–10094. https://doi.org/10.5194/acp-13-10081-2013.
Fick, S.E., Hijmans, R.J., 2017. WorldClim 2: New 1-km spatial resolution climate surfaces for global land areas. Int. J. Climatol. 37, 4302–4315. https://doi.org/10.1002/joc.5086.
Finstad, K., Pfeiffer, M., Amundson, R., 2014. Hyperarid soils and the soil taxonomy. Soil Sci. Soc. Am. J. 78, 1845–1851. https://doi.org/10.2136/sssaj2014.06.0247.
Fletcher, L.E., Valdivia-Silva, J.E., Perez-Montaño, S., Condori-Apaza, R.M., Conley, C.A., McKay, C.P., 2012. Variability of organic material in surface horizons of the hyper-arid Mars-like soils of the Atacama Desert. Adv. Space Res. 49, 271–279. https://doi.org/10.1016/j.asr.2011.10.001.
Frankel, K.L., Dolan, J.F., 2007. Characterizing arid region alluvial fan surface roughness with airborne laser swath mapping digital topographic data. J. Geophys. Res. 112, F02025. https://doi.org/10.1029/2006JF000644.
Fuentes, B., Choque, A., Gómez, F., Alarcón, J., Castro-Nallar, E., Arenas, F., Contreras, D., Mörchen, R., Amelung, W., Knief, C., Moradi, G., Klumpp, E., Saavedra, C.P., Prietzel, J., Klysubun, W., Remonsellez, F., Bol, R., 2022a. Influence of physical-chemical soil parameters on microbiota composition and diversity in a deep hyperarid core of the Atacama Desert. Front. Microbiol. 12, 794743 https://doi.org/10.3389/fmicb.2021.794743.
Fuentes, B., Gómez, F., Valdez, C., Videla, A., Castro-Severyn, J., Barahona, S., Bol, R., Riquelme, R., Quispe, J., Remonsellez, F., 2022b. Effects of altitude on soil properties in coastal fog ecosystems in Morro Moreno National Park, Antofagasta. Chile. European Journal of Soil Science 73, e13217.
Fuenzalida, H.A., Sánchez, R., Garreaud, R.D., 2005. A climatology of cutoff lows in the Southern Hemisphere. J. Geophys. Res. 110, D18101. https://doi.org/10.1029/2005JD005934.
García-Pérez, T., Marquardt, C., Yáñez, G., Cembrano, J., Gomila, R., Santibañez, I., Maringue, J., 2018. Insights on the structural control of a Neogene forearc basin in Northern Chile: A geophysical approach. Tectonophysics 736, 1–14. https://doi.org/10.1016/j.tecto.2018.04.003.
Gardner, R., Pye, K., 1981. Nature, origin and palaeoenvironmental significance of red coastal and desert dune sands. Progress in Physical Geography: Earth and Environment 5, 514–534. https://doi.org/10.1177/030913338100500402.
Garreaud, R., Barichivich, J., Christie, D.A., Maldonado, A., 2008. Interannual variability of the coastal fog at Fray Jorge relict forests in semiarid Chile. J. Geophys. Res. 113, G04011. https://doi.org/10.1029/2008JG000709.
Garreaud, R.D., Vuille, M., Compagnucci, R., Marengo, J., 2009. Present-day South American climate. Palaeogeogr. Palaeoclimatol. Palaeoecol. 281, 180–195. https://doi.org/10.1016/j.palaeo.2007.10.032.
González, G., Cembrano, J., Carrizo, D., Macci, A., Schneider, H., 2003. The link between forearc tectonics and Pliocene-Quaternary deformation of the Coastal Cordillera, northern Chile. J. S. Am. Earth Sci. 16, 321–342. https://doi.org/10.1016/S0895-9811(03)00100-7.
Graham, D.J., Midgley, N.G., 2000. Graphical representation of particle shape using triangular diagrams: An excel spreadsheet method. Earth Surf. Proc. Land. 25, 1473–1477. https://doi.org/10.1002/1096-9837(200012)25:13<1473::aid-esp158>3.0.co;2-c.
Gray, J.M., Humphreys, G.S., Deckers, J.A., 2011. Distribution patterns of World Reference Base soil groups relative to soil forming factors. Geoderma 160, 373–383. https://doi.org/10.1016/j.geoderma.2010.10.006.
Grocott, J., Taylor, G.K., 2002. Magmatic arc fault systems, deformation partitioning and emplacement of granitic complexes in the Coastal Cordillera, north Chilean Andes (25°30′S to 27°00′S). J. Geol. Soc. London 159, 425–443. https://doi.org/10.1144/0016-764901-124.
Hartley, A.J., May, G., Chong, G., Turner, P., Kape, S.J., Jolley, E.J., 2000. Development of a continental forearc: A Cenozoic example from the Central Andes, northern Chile. Geology 28, 331–334. https://doi.org/10.1130/0091-7613(2000)28<331:DOACFA>2.0.CO;2.
Hartley, A.J., Mather, A.E., Jolley, E., Turner, P., 2005. Climatic controls on alluvial-fan activity, Coastal Cordillera, northern Chile. Geol. Soc. Lond. Spec. Publ. 251, 95–116. https://doi.org/10.1144/GSL.SP.2005.251.01.08.
Harvey, A.M., Foster, G., Hannam, J., Mather, A.E., 2003. The Tabernas alluvial fan and lake system, southeast Spain: applications of mineral magnetic and pedogenic iron oxide analyses towards clarifying the Quaternary sediment sequences. Geomorphology 50, 151–171. https://doi.org/10.1016/S0169-555X(02)00212-X.
Haschke, M., Siebel, W., Günther, A., Scheuber, E., 2002. Repeated crustal thickening and recycling during the Andean orogeny in north Chile (21°–26°S). Journal of Geophysical Research: Solid Earth 107, ECV 6-1–ECV 6-18. Doi:10.1029/2001JB000328.
Hirsch, F., Raab, T., Błaszkiewicz, M., 2021. Evidence for an alternative concept of the Finow soil formation. Catena 198, 105064. https://doi.org/10.1016/j.catena.2020.105064.
Hoffmeister, D., 2018. Meteorological and soil measurements of the permanent weather stations in the Atacama desert, Chile. CRC1211 Database (CRC1211DB). https://doi.org/10.5880/CRC1211DB.1.

Holmgren, G.G.S., 1967. A rapid citrate-dithionite extractable iron procedure. Soil Sci. Soc. Am. J. 31, 210–211. https://doi.org/10.2136/sssaj1967.03615995003100020020x.

Houston, J., 2006. Variability of precipitation in the Atacama Desert: its causes and hydrological impact. Int. J. Climatol. 26, 2181–2198. https://doi.org/10.1002/joc.1359.

International Union of Soil Sciences (IUSS) Working Group WRB, 2022. World Reference Base for Soil Resources: International soil classification system for naming soils and creating legends for soil maps, 4th edition. IUSS, Vienna.

ISO 10693, 1995. Soil quality - Determination of carbonate content - Volumetric method. International Organization for Standardization, Geneva.

Jahn, R., Blume, H.P., Asio, V.B., Spaargaren, O., Schad, P., 2006. Guidelines for soil description, 4th edition. Food and Agriculture Organization of the United Nations, Rome.

Jordan, T.E., Kirk-Lawlor, N.E., Blanco, N.P., Rech, J.A., Cosentino, N.J., 2014. Landscape modification in response to repeated onset of hyperarid paleoclimate states since 14 Ma, Atacama Desert, Chile. GSA Bull. 126, 1016–1046. https://doi.org/10.1130/B30978.1.

Jordan, T.E., Herrera, C., Godfrey, L.V., Colucci, S.J., Gamboa, C., Urrutia, J., González, G., Paul, J.F., 2018. Isotopic characteristics and paleoclimate implications of the extreme rain event of March 2015 in northern Chile. Andean Geol. 46, 1–31. https://doi.org/10.5027/andgeoV46n1-3087.

Knief, C., Bol, R., Amelung, W., Kusch, S., Frindte, K., Eckmeier, E., Jaeschke, A., Dunai, T., Fuentes, B., Mörchen, R., Schütte, T., Lücke, A., Klumpp, E., Kaiser, K., Rethemeyer, J., 2020. Tracing elevational changes in microbial life and organic carbon sources in soils of the Atacama Desert. Global Planet. Change 184, 103078. https://doi.org/10.1016/j.gloplacha.2019.103078.

Kohl, C.P., Nishiizumi, K., 1992. Chemical isolation of quartz for measurement of in-situ -produced cosmogenic nuclides. Geochim. Cosmochim. Acta 56, 3583–3587. https://doi.org/10.1016/0016-7037(92)90401-4.

Kooistra, M.J., Pulleman, M.M., 2018. Chapter 16 – Features Related to Faunal Activity. In: Stoops, G., Marcelino, V., Mees, F. (Eds.), Interpretation of Micromorphological Features of Soils and Regoliths, 2nd edition. Elsevier, Amsterdam, pp. 447–469.

Kuhlman, K.R., Venkat, P., La Duc, M.T., Kuhlman, G.M., McKay, C.P., 2008. Evidence of a microbial community associated with rock varnish at Yungay, Atacama Desert. Chile. Journal of Geophysical Research 113, G04022. https://doi.org/10.1029/2007JG000677.

Lafon, S., Rajot, J.-L., Alfaro, S.C., Gaudichet, A., 2004. Quantification of iron oxides in desert aerosol. Atmos. Environ. 38, 1211–1218. https://doi.org/10.1016/j.atmosenv.2003.11.006.

Lamy, F., Klump, J., Hebbeln, D., Wefer, G., 2000. Late Quaternary rapid climate change in northern Chile. Terra Nova 12, 8–13. https://doi.org/10.1046/j.1365-3121.2000.00265.x.

Li, J., Wang, F., Michalski, G., Wilkins, B., 2019. Atmospheric deposition across the Atacama Desert, Chile: Compositions, source distributions, and interannual comparisons. Chem. Geol. 525, 435–446. https://doi.org/10.1016/j.chemgeo.2019.07.037.

Lifton, N., Sato, T., Dunai, T.J., 2014. Scaling *in situ* cosmogenic nuclide production rates using analytical approximations to atmospheric cosmic-ray fluxes. Earth Planet. Sci. Lett. 386, 149–160. https://doi.org/10.1016/j.epsl.2013.10.052.

Lisiecki, L.E., Raymo, M.E., 2005. A Pliocene-Pleistocene stack of 57 globally distributed benthic $\delta^{18}O$ records. Paleoceanography 20, 1–17. https://doi.org/10.1029/2004PA001071.

Lucke, B., Sprafke, T., 2015. Correlation of soil color, redness ratings, and weathering indices of Terrae Calcis along a precipitation gradient in northern Jordan. In: Lucke, B., Bäumler, R., Schmidt, M. (Eds.), Soils and sediments as archives of environmental change. Geoarchaeology and landscape change in the subtropics and tropics, Fränkische Geographische Gesellschaft, Erlangen, pp. 53–68.

Marquardt, C., 2005. Déformations Néogènes le long de la Côte Nord du Chili (23°–27° S), Avant-Arc des Andes Centrales. In: Laboratoire des Mécanismes et Transfert en Géologie. Université Toulouse III – Paul Sabatier, Toulouse, France, p. 212 pp.,. PhD thesis,.

Martínez, M.L., Intralawan, A., Vázquez, G., Pérez-Maqueo, O., Sutton, P., Landgrave, R., 2007. The coasts of our world: Ecological, economic and social importance. Ecol. Econ. 63, 254–272. https://doi.org/10.1016/j.ecolecon.2006.10.022.

Mason, B.H., Moore, C.B., 1982. Principles of Geochemistry, 4th edition. Wiley, New York, USA.

May, S.M., Meine, L., Hoffmeister, D., Brill, D., Medialdea, A., Wennrich, V., Gröbner, M., Schulte, P., Steininger, F., Deprez, M., de Kock, T., Bubenzer, O., 2020. Origin and timing of past hillslope activity in the hyper-arid core of the Atacama Desert – The formation of fine sediment lobes along the Chuculay Fault System. Northern Chile. Global and Planetary Change 184, 103057. https://doi.org/10.1016/j.gloplacha.2019.103057.

McAuliffe, J.R., McFadden, L.D., Hoffman, M.T., 2018. Role of aeolian dust in shaping landscapes and soils of arid and semi-arid South Africa. Geosciences 8, 171. https://doi.org/10.3390/geosciences8050171.

Medialdea, A., May, S.M., Brill, D., King, G., Ritter, B., Wennrich, V., Bartz, M., Zander, A., Kuiper, K., Hurtado, S., Hoffmeister, D., Schulte, P., Gröbner, M., Opitz, S., Brückner, H., Bubenzer, O., 2020. Identification of humid periods in the Atacama Desert through hillslope activity established by infrared stimulated luminescence (IRSL) dating. Global Planet. Change 185, 103086. https://doi.org/10.1016/j.gloplacha.2019.103086.

Mehra, O.P., Jackson, M.L., 1958. Iron oxide removal from soils and clays by a dithionite-citrate system buffered with sodium bicarbonate. Clay Clay Miner. 7, 317–327. https://doi.org/10.1346/CCMN.1958.0070122.

Middleton, N.J., Thomas, D.S.G. (Eds.), 1997. World Atlas of Desertification, 2nd ed. Edward Arnold, London.

Molina, F.V., 2013. Soil Colloids: Properties and Ion Binding. CRC Press, Boca Raton. https://doi.org/10.1201/b15349.

Moradi, G., Bol, R., Trbojevic, L., Missong, A., Mörchen, R., Fuentes, B., May, S.M., Lehndorff, E., Klumpp, E., 2020. Contrasting depth distribution of colloid-associated phosphorus in the active and abandoned sections of an alluvial fan in a hyper-arid region of the Atacama Desert. Global Planet. Change 185, 103090. https://doi.org/10.1016/j.gloplacha.2019.103090.

Mörchen, R., Lehndorff, E., Arenas Diaz, F., Moradi, G., Bol, R., Fuentes, B., Klumpp, E., Amelung, W., 2019. Carbon accrual in the Atacama Desert. Global Planet. Change 181, 102993. https://doi.org/10.1016/j.gloplacha.2019.102993.

Mörchen, R., Amelung, W., Giese, C., Böhnert, T., Ruhm, J., Lehndorff, E., 2021. Fingerprint of plant life in the Atacama Desert – Insights from *n*-alkane analyses. Org Geochem. 151, 104145 https://doi.org/10.1016/j.orggeochem.2020.104145.

Nagano, T., Nakashima, S., Nakayama, S., Senoo, M., 1994. The use of color to quantify the effects of pH and temperature on the crystallization kinetics of goethite under highly alkaline conditions. Clay Clay Miner. 42, 226–234. https://doi.org/10.1346/CCMN.1994.0420213.

Nettleton, W.D., Peterson, F.F., 1983. Aridisols. In: Wilding, L.P., Smeck, N.E., Hall, G.F. (Eds.), Pedogenesis and Soil Taxonomy. II. The Soil Orders, Elsevier, Amsterdam, pp. 165–215.

Nishiizumi, K., Imamura, M., Caffee, M.W., Southon, J.R., Finkel, R.C., McAninch, J., 2007. Absolute calibration of ^{10}Be AMS standards. Nucl. Instrum. Methods Phys. Res., Sect. B 258, 403–413. https://doi.org/10.1016/j.nimb.2007.01.297.

Oliveros, V., González, J., Espinoza Vargas, M., Vásquez, P., Rossel, P., Creixell, C., Sepúlveda, F., Bastias, F., 2018. The early stages of the magmatic arc in the southern Central Andes. In: Folguera, A., Contreras-Reyes, E., Heredia, N., Encinas, A., Iannelli, S.B., Oliveros, V., Dávila, F.M., Collo, G., Giambiagi, L., Maksymowicz, A., Iglesia Llanos, M.P., Turienzo, M., Naipauer, M., Orts, D., Litvak, V.D., Alvarez, O., Arriagada, C. (eds.) The Evolution of the Chilean-Argentinean Andes. Springer International Publishing, Cham, 165–190. Doi:10.1007/978-3-319-67774-3_7.

Owen, L.A., Clemmens, S.J., Finkel, R.C., Gray, H., 2014. Late Quaternary alluvial fans at the eastern end of the San Bernardino Mountains, Southern California. Quat. Sci. Rev. 87, 114–134. https://doi.org/10.1016/j.quascirev.2014.01.003.

Özer, M., Orhan, M., Işik, N.S., 2010. Effect of particle optical properties on size distribution of soils obtained by laser diffraction. Environ. Eng. Geosci. 16, 163–173. https://doi.org/10.2113/gseegeosci.16.2.163.

Parro, V., de Diego-Castilla, G., Moreno-Paz, M., Blanco, Y., Cruz-Gil, P., Rodríguez-Manfredi, J.A., Fernández-Remolar, D., Gómez, F., Gómez, M.J., Rivas, L.A., Demergasso, C., Echeverría, A., Urtuvia, V.N., Ruiz-Bermejo, M., García-Villadangos, M., Postigo, M., Sánchez-Román, M., Chong-Díaz, G., Gómez-Elvira, J., 2011. A microbial oasis in the hypersaline Atacama subsurface discovered by a life detector chip: implications for the search for life on Mars. Astrobiology 11, 969–996. https://doi.org/10.1089/ast.2011.0654.

Placzek, C., Granger, D.E., Matmon, A., Quade, J., Ryb, U., 2014. Geomorphic process rates in the central Atacama Desert, Chile: Insights from cosmogenic nuclides and implications for the onset of hyperaridity. Am. J. Sci. 314, 1462–1512. https://doi.org/10.2475/10.2014.03.

Placzek, C.J., Matmon, A., Granger, D.E., Quade, J., Niedermann, S., 2010. Evidence for active landscape evolution in the hyperarid Atacama from multiple terrestrial cosmogenic nuclides. Earth Planet. Sci. Lett. 295, 12–20. https://doi.org/10.1016/j.epsl.2010.03.006.

Quade, J., Rech, J.A., Latorre, C., Betancourt, J.L., Gleeson, E., Kalin, M.T.K., 2007. Soils at the hyperarid margin: The isotopic composition of soil carbonate from the Atacama Desert, Northern Chile. Geochim. Cosmochim. Acta 71, 3772–3795. https://doi.org/10.1016/j.gca.2007.02.016.

Rech, J.A., Quade, J., Hart, W.S., 2003. Isotopic evidence for the source of Ca and S in soil gypsum, anhydrite and calcite in the Atacama Desert, Chile. Geochim. Cosmochim. Acta 67, 575–586. https://doi.org/10.1016/S0016-7037(02)01175-4.

Regard, V., Saillard, M., Martinod, J., Audin, L., Carretier, S., Pedoja, K., Riquelme, R., Paredes, P., Hérail, G., 2010. Renewed uplift of the Central Andes Forearc revealed by coastal evolution during the Quaternary. Earth Planet. Sci. Lett. 297, 199–210. https://doi.org/10.1016/j.epsl.2010.06.020.

Reheis, M.C., Goodmacher, J.C., Harden, J.W., McFadden, L.D., Rockwell, T.K., Shroba, R.R., Sowers, J.M., Taylor, E.M., 1995. Quaternary soils and dust deposition in southern Nevada and California. GSA Bull. 107, 1003–1022. https://doi.org/10.1130/0016-7606(1995)107<1003:QSADDI>2.3.CO;2.

Reiniger, P., Bolt, G.H., 1972. Theory of chromatography and its application to cation exchange in soils. Neth. J. Agric. Sci. 20, 301–313. https://doi.org/10.18174/njas.v20i4.17277.

Reyers, M., Hamidi, M., Shao, Y., 2019. Synoptic analysis and simulation of an unusual dust event over the Atacama Desert. Atmos. Sci. Lett. 20, e899.

Reyers, M., Boehm, C., Knarr, L., Shao, Y., Crewell, S., 2021. Synoptic-to-regional-scale analysis of rainfall in the Atacama Desert (18°–26°S) using a long-term simulation with WRF. Mon. Weather Rev. 149, 91–112. https://doi.org/10.1175/MWR-D-20-0038.1.

Reyers, M., Shao, Y., 2019. Cutoff lows off the coast of the Atacama Desert under present day conditions and in the Last Glacial Maximum. Global Planet. Change 181, 102983. https://doi.org/10.1016/j.gloplacha.2019.102983.

Rincón-Martínez, D., Lamy, F., Contreras, S., Leduc, G., Bard, E., Saukel, C., Blanz, T., Mackensen, A., Tiedemann, R., 2010. More humid interglacials in Ecuador during the past 500 kyr linked to latitudinal shifts of the equatorial front and the Intertropical Convergence Zone in the eastern tropical Pacific. Paleoceanography 25, 1–15. https://doi.org/10.1029/2009PA001868.

Ritter, B., Stuart, F.M., Binnie, S.A., Gerdes, A., Wennrich, V., Dunai, T.J., 2018. Neogene fluvial landscape evolution in the hyperarid core of the Atacama Desert. Sci. Rep. 8, 13952. https://doi.org/10.1038/s41598-018-32339-9.

Ritter, B., Wennrich, V., Medialdea, A., Brill, D., King, G., Schneiderwind, S., Niemann, K., Fernández-Galego, E., Diederich, J., Rolf, C., Bao, R., Melles, M., Dunai, T.J., 2019. Climatic fluctuations in the hyperarid core of the Atacama Desert during the past 215 ka. Sci. Rep. 9, 5270. https://doi.org/10.1038/s41598-019-41743-8.

Ritz, J.-F., Braucher, R., Bourlès, D., Delouis, B., Marquardt, C., Lavenu, A., Philip, H., Ortlieb, L., 2019. Slip rate of trench-parallel normal faulting along the Mejillones Fault (Atacama Fault System): Relationships with the northern Chile subduction and implications for seismic hazards. Terra Nova 31, 390–404. https://doi.org/10.1111/ter.12401.

Rondanelli, R., Hatchett, B., Rutllant, J., Bozkurt, D., Garreaud, R., 2019. Strongest MJO on record triggers extreme Atacama rainfall and warmth in Antarctica. Geophys. Res. Lett. 46, 3482–3491. https://doi.org/10.1029/2018GL081475.

Rowell, D.L., 1994. Soil Science: Methods and Applications. Longman, Harlow.

Rundel, P.W., Dillon, M.O., Palma, B., Mooney, H.A., Gulmon, S.L., Ehleringer, J.R., 1991. The phytogeography and ecology of the coastal Atacama and Peruvian Deserts. Aliso: A Journal of Systematic and Floristic Botany 13, 2. https://doi.org/10.5642/aliso.19911301.02.

Rundel, P.W., Mahu, M., 1976. Community structure and diversity in a coastal fog desert in northern Chile. Flora 165, 493–505. https://doi.org/10.1016/S0367-2530(17)31888-1.

Saha, S., Owen, L.A., Orr, E.N., Caffee, M.W., 2018. Timing and nature of Holocene glacier advances at the northwestern end of the Himalayan-Tibetan Orogen. Quat. Sci. Rev. 187, 177–202. https://doi.org/10.1016/j.quascirev.2018.03.009.

Sahwan, W., Lucke, B., Sprafke, T., Vanselow, K.A., Bäumler, R., 2021. Relationships between spectral features, iron oxides and colours of surface soils in northern Jordan. Eur. J. Soil Sci. 72, 80–97. https://doi.org/10.1111/ejss.12986.

Schaller, K., 2000. Praktikum zur Bodenkunde und Pflanzenernährung, 8th ed. Forschungsanstalt Geisenheim, Geisenheim.

Scheuber, E., González, G., 1999. Tectonics of the Jurassic-Early Cretaceous magmatic arc of the north Chilean Coastal Cordillera (22°–26°S): A story of crustal deformation along a convergent plate boundary. Tectonics 18, 895–910. https://doi.org/10.1029/1999TC900024.

Schulte, P., Hamacher, H., Lehmkuhl, F., Esser, V., 2022. Initial soil formation in an artificial river valley - Interplay of anthropogenic landscape shaping and fluvial dynamics. Geomorphology 398, 108064. https://doi.org/10.1016/j.geomorph.2021.108064.

Schulte, P., Lehmkuhl, F., 2018. The difference of two laser diffraction patterns as an indicator for post-depositional grain size reduction in loess-paleosol sequences. Palaeogeogr. Palaeoclimatol. Palaeoecol. 509, 126–136. https://doi.org/10.1016/j.palaeo.2017.02.022.

Schulte, P., Lehmkuhl, F., Steininger, F., Loibl, D., Lockot, G., Protze, J., Fischer, P., Stauch, G., 2016. Influence of HCl pretreatment and organo-mineral complexes on laser diffraction measurement of loess-paleosol-sequences. Catena 137, 392–405. https://doi.org/10.1016/j.catena.2015.10.015.

Schulz, N., Aceituno, P., Richter, M., 2011. Phytogeographic divisions, climate change and plant dieback along the coastal desert of northern Chile. Erdkunde 65, 169–187. https://doi.org/10.3112/erdkunde.2011.02.05.

Schulz, N., 2009. Loma-Formationen der Küsten-Atacama/Nordchile unter besonderer Berücksichtigung rezenter Vegetations- und Klimaveränderungen. Dissertation, Friedrich-Alexander University Erlangen-Nürnberg, Erlangen. URN: urn:nbn:de:bvb:29-opus-12894. URL: https://opus4.kobv.de/opus4-fau/frontdoor/index/index/docId/829 (Accessed 27 December 2022).

Schween, J.H., Hoffmeister, D., Löhnert, U., 2020. Filling the observational gap in the Atacama Desert with a new network of climate stations. Global Planet. Change 184, 103034. https://doi.org/10.1016/j.gloplacha.2019.103034.

Schween, J.H., del Río, C., García, J.-L., Osses, P., Westbrook, S., Löhnert, U., 2022. Life cycle of stratocumulus clouds over 1 year at the coast of the Atacama Desert. Atmos. Chem. Phys. 22, 12241–12267. https://doi.org/10.5194/acp-22-12241-2022.

Schwertmann, U., 1959. Die fraktionierte Extraktion der freien Eisenoxyde in Böden, ihre mineralogischen Formen und ihre Entstehungsweisen. J. Plant Nutr. Soil Sci. 84, 194–204. https://doi.org/10.1002/jpln.19590840131.

Schwertmann, U., Murad, E., 1983. Effect of pH on the formation of goethite and hematite from ferrihydrite. Clay Clay Miner. 31, 277–284. https://doi.org/10.1346/CCMN.1983.0310405.

Schwertmann, U., Murad, E., Schulze, D.G., 1983. Is there Holocene reddening (hematite formation) in soils of axeric temperate areas? Geoderma 27, 209–223. https://doi.org/10.1016/0016-7061(82)90031-3.

Shackleton, N.J., Pisias, N.G., 1985. Atmospheric carbon dioxide, orbital forcing, and climate. In: Sundquist, E.T., Broecker, W.S. (eds.) The Carbon Cycle and Atmospheric C02: Natural Variations Archean to Present. American Geophysical Union, Geophysical Monograph 32, 303–317.

Sheldon, N.D., Tabor, N.J., 2009. Quantitative paleoenvironmental and paleoclimatic reconstruction using paleosols. Earth Sci. Rev. 95, 1–52. https://doi.org/10.1016/j.earscirev.2009.03.004.

Siddall, M., Chappell, J., Potter, E.K., 2007. Eustatic sea level during past interglacials. In: Sirocko, F., Litt, T., Claussen, M., Sanchez-Goni, M.-.-F. (Eds.), The Climate of Past Interglacials. Elsevier, Amsterdam, pp. 75–92. https://doi.org/10.1016/S1571-0866(07)80032-7.

Soil Survey Staff, 1999. Soil taxonomy: A basic system of soil classification for making and interpreting soil surveys, 2nd edition. Agricultural Handbook 436. Natural Resources Conservation Service, United States Department of Agriculture, Washington, DC.

SPECTRO (ed.), 2007. Analysis of Trace Elements in Geological Materials, Soils and Sludges Prepared as Pressed Pellets. SPECTRO XRF Report.

Spelz, R.M., Fletcher, J.M., Owen, L.A., Caffee, M.W., 2008. Quaternary alluvial-fan development, climate and morphologic dating of fault scarps in Laguna Salada, Baja California, Mexico. Geomorphology 102, 578–594. https://doi.org/10.1016/j.geomorph.2008.06.001.

Stevens, P.R., Walker, T.W., The chronosequence concept and soil formation. The Quaterly Review of Biology 45, 333–350. https://www.jstor.org/stable/2821008.

Stone, J., Fifield, K., Beer, J., Vonmoos, M., Obrist, C., Grajcar, M., Kubik, P., Muscheler, R., Finkel, R., Caffee, M., 2004. Co-precipitated silver-metal oxide aggregates for accelerator mass spectrometry of ^{10}Be and ^{26}Al. Nucl. Instrum. Methods Phys. Res., Sect. B 223–224, 272–277. https://doi.org/10.1016/j.nimb.2004.04.055.

Stoops, G., 2021. Guidelines for Analysis and Description of Regolith Thin Sections, 2nd ed. John Wiley & Sons, Hoboken, NJ.

Stoops, G., Marcelino, V., Mees, F. (Eds.), 2018. Interpretation of Micromorphological Features of Soils and Regoliths, 2nd ed. Elsevier, Amsterdam.

Sträter, E., Westbeld, A., Klemm, O., 2010. Pollution in coastal fog at Alto Patache, Northern Chile. Environ. Sci. Pollut. Res. 17, 1563–1573. https://doi.org/10.1007/s11356-010-0343-x.

Stuut, J.B.W., Lamy, F., 2004. Climate variability at the southern boundaries of the Namib (southwestern Africa) and Atacama (northern Chile) coastal deserts during the last 120,000 yr. Quat. Res. 62, 301–309. https://doi.org/10.1016/j.yqres.2004.08.001.

Thomas, G.W., Hargrove, W.L., 1984. The Chemistry of Soil Acidity. In: Adams, F. (Ed.), Soil Acidity and Liming, 2nd edition. American Society of Agronomy, Inc., Crop Science Society of America, Inc. Soil Science Society of America, Madison, pp. 3–56. https://doi.org/10.2134/agronmonogr12.2ed.

Tofelde, S., Duesing, W., Schildgen, T.F., Wickert, A.D., Wittmann, H., Alonso, R.N., Strecker, M., 2018. Effects of deep-seated versus shallow hillslope processes on cosmogenic ^{10}Be concentrations in fluvial sand and gravel. Earth Surf. Proc. Land. 43, 3086–3098. https://doi.org/10.1002/esp.4471.

Trabucco, A., Zomer, R.J., 2019. Global Aridity Index and Potential Evapotranspiration (ET0) Climate Database v2 (Global_AI_PET_v2). figshare. Doi:10.6084/m9.figshare.7504448.v3.

United States Department of Agriculture (USDA), 1987. Soil Mechanics Level I, Module 3 – USDA Textural Soil Classification: Study Guide. Soil Conservation Service, USDA.

United States Geological Survey (USGS), 2014. Shuttle Radar Topography Mission (SRTM) 1 Arc-Second Global. USGS EROS Archive. Doi:10.5066/F7PR7TFT.

Valdivia-Silva, J.E., Navarro-González, R., Fletcher, L., Perez-Montaño, S., Condori-Apaza, R.M., McKay, C.P., 2012. Soil carbon distribution and site characteristics in hyper-arid soils of the Atacama Desert: A site with Mars-like soils. Adv. Space Res. 50, 108–122. https://doi.org/10.1016/j.asr.2012.03.003.

van Asten, P.J.A., van 't Zelfde, J.A., van der Zee, S.E.A.T.M., Hammecker, C., 2004. The effect of irrigated rice cropping on the alkalinity of two alkaline rice soils in the Sahel. Geoderma 119, 233–247. Doi:10.1016/j.geoderma.2003.08.002.

van Breemen, N., Mulder, J., Driscoll, C.T., 1983. Acidification and alkalinization of soils. Plant and Soil 75, 283–308. https://doi.org/10.1007/BF02369968.

van Dongen, R., Scherler, D., Wittmann, H., Von Blanckenburg, F., 2019. Cosmogenic ^{10}Be in river sediment: where grain size matters and why. Earth Surf. Dyn. 7, 393–410. https://doi.org/10.5194/esurf-7-393-2019.

Vargas, G., Rutllant, J., Ortlieb, L., 2006. ENSO tropical–extratropical climate teleconnections and mechanisms for Holocene debris flows along the hyperarid coast of western South America (17°–24°S). Earth Planet. Sci. Lett. 249, 467–483. https://doi.org/10.1016/j.epsl.2006.07.022.

Ventra, D., Clarke, L.E., 2018. Geology and geomorphology of alluvial and fluvial fans: Current progress and research perspectives. In: Ventra, D., Clarke, L.E. (Eds.), Geology and Geomorphology of Alluvial and Fluvial Fans: Terrestrial and Planetary Perspectives. Geological Society, 440. Special Publications, London, pp. 1–22. https://doi.org/10.1144/SP440.16.

Viscarra Rossel, R.A., Cattle, S.R., Ortega, A., Fouad, Y., 2009. In situ measurements of soil colour, mineral composition and clay content by Vis–NIR spectroscopy. Geoderma 150, 253–266. https://doi.org/10.1016/j.geoderma.2009.01.025.

Voigt, C., Klipsch, S., Herwartz, D., Chong, G., Staubwasser, M., 2020. The spatial distribution of soluble salts in the surface soil of the Atacama Desert and their relationship to hyperaridity. Global Planet. Change 184, 103077. https://doi.org/10.1016/j.gloplacha.2019.103077.

Vuille, M., Ammann, C., 1997. Regional snowfall patterns in the high, arid Andes. Clim. Change 36, 413–423. https://doi.org/10.1023/A:1005330802974.

Wagner, S., Eckmeier, E., Skowronek, A., Günster, N., 2014. Quaternary paleosols and sediments on the Balearic Islands as indicators of climate changes. Catena 112, 112–124. https://doi.org/10.1016/j.catena.2013.06.022.

Walk, J., Stauch, G., Bartz, M., Brückner, H., Lehmkuhl, F., 2019. Geomorphology of the coastal alluvial fan complex Guanillos, northern Chile. J. Maps 15, 436–447. https://doi.org/10.1080/17445647.2019.1611499.

Walk, J., Stauch, G., Reyers, M., Vásquez, P., Sepúlveda, F.A., Bartz, M., Hoffmeister, D., Brückner, H., Lehmkuhl, F., 2020. Gradients in climate, geology, and topography affecting coastal alluvial fan morphodynamics in hyperarid regions – The Atacama perspective. Global Planet. Change 185, 102994. https://doi.org/10.1016/j.gloplacha.2019.102994.

Walk, J., Bartz, M., Stauch, G., Binnie, A., Brückner, H., Lehmkuhl, F., 2022. Weathering under coastal hyperaridity – Late Quaternary development of spec-tral, textural, and gravelometric alluvial fan surface characteristics. Quat. Sci. Rev. 277, 107339 https://doi.org/10.1016/j.quascirev.2021.107339.

Walk, J., 2022. UAS-based very high resolution digital elevation model and orthomosaic of the coastal alluvial fan Paposo, Atacama Desert. CRC1211 Database

(CRC1211DB). URL: https://www.crc1211db.uni-koeln.de/search/view.php?dataID=651. (Accessed 20 December 2022).
Wang, F., Michalski, G., Seo, J., Ge, W., 2014. Geochemical, isotopic, and mineralogical constraints on atmospheric deposition in the hyper-arid Atacama Desert, Chile. Geochim. Cosmochim. Acta 135, 29–48. https://doi.org/10.1016/j.gca.2014.03.017.
Warren-Rhodes, K.A., Lee, K.C., Archer, S.D.J., Cabrol, N., Ng-Boyle, L., Wettergreen, D., Zacny, K., Pointing, S.B., the NASA Life in the Atacama Project Team, 2019. Subsurface microbial habitats in an extreme desert Mars-analog environment. Front. Microbiol. 10, 69. Doi:10.3389/fmicb.2019.00069.
Wells, S.G., McFadden, L.D., Schultz, J.D., 1990. Eolian landscape evolution and soil formation in the Chaco dune field, southern Colorado Plateau, New Mexico. Geomorphology 3, 517–546. https://doi.org/10.1016/0169-555X(90)90019-M.
Wierzchos, J., Cámara, B., de Los Ríos, A., Davila, A.F., Sánchez Almazo, I.M., Artieda, O., Wierzchos, K., Gómez-Silva, B., McKay, C., Ascaso, C., 2011. Microbial colonization of Ca-sulfate crusts in the hyperarid core of the Atacama Desert: implications for the search for life on Mars. Geobiology 9, 44–60. https://doi.org/10.1111/j.1472-4669.2010.00254.x.
Williams, A.J., Pagliai, M., Stoops, G., 2018. Chapter 19 – Physical and Biological Surface Crusts and Seals. In: Stoops, G., Marcelino, V., Mees, F. (Eds.), Interpretation of Micromorphological Features of Soils and Regoliths, 2nd edition. Elsevier, Amsterdam, pp. 539–574.
Yang, Q., Li, X., Han, Z., Wang, X., Zhao, W., Yi, S., Lu, H., 2022. DCB dissolution of iron oxides in aeolian dust deposits controlled by particle size rather than mineral species. Sci. Rep. 12, 2786. https://doi.org/10.1038/s41598-022-06734-2.
Zeeden, C., Krauß, L., Kels, H., Lehmkuhl, F., 2017. Digital image analysis of outcropping sediments: Comparison to photospectrometric data from Quaternary loess deposits at Șanoviț a (Romania) and Achenheim (France). Quat. Int. 429, 100–107. https://doi.org/10.1016/j.quaint.2016.02.047.